Journal of Computational Physics 274 (2014) 64–94

Contents lists available at ScienceDirect

Journal of Computational Physics

www.elsevier.com/locate/jcp

Simulation of confined magnetohydrodynamic flows with Dirichlet boundary conditions using a pseudo-spectral method with volume penalization

Jorge A. Morales [a,*], Matthieu Leroy [b], Wouter J.T. Bos [a], Kai Schneider [b]

[a] LMFA-CNRS, École Centrale de Lyon, Université de Lyon, France
[b] M2P2-CNRS, Aix-Marseille Université, Marseille, France

ARTICLE INFO

Article history:
Received 20 August 2013
Received in revised form 16 April 2014
Accepted 28 May 2014
Available online 2 June 2014

Keywords:
MHD
Immersed boundary
Penalization method
Pseudo-spectral
Hartmann-instabilities
Helical magnetic field
Taylor–Couette

ABSTRACT

A volume penalization approach to simulate magnetohydrodynamic (MHD) flows in confined domains is presented. Here the incompressible visco-resistive MHD equations are solved using parallel pseudo-spectral solvers in Cartesian geometries. The volume penalization technique is an immersed boundary method which is characterized by a high flexibility for the geometry of the considered flow. In the present case, it allows to use other than periodic boundary conditions in a Fourier pseudo-spectral approach. The numerical method is validated and its convergence is assessed for two- and three-dimensional hydrodynamic (HD) and MHD flows, by comparing the numerical results with results from literature and analytical solutions. The test cases considered are two-dimensional Taylor–Couette flow, the *z*-pinch configuration, three dimensional Orszag–Tang flow, Ohmic-decay in a periodic cylinder, three-dimensional Taylor–Couette flow with and without axial magnetic field and three-dimensional Hartmann-instabilities in a cylinder with an imposed helical magnetic field. Finally, we present a magnetohydrodynamic flow simulation in toroidal geometry with non-symmetric cross section and imposing a helical magnetic field to illustrate the potential of the method.

1. Introduction

Magnetohydrodynamics is the discipline that studies the interaction between conducting fluids and magnetic fields. Depending on the topology and the intensity of the magnetic field, as well as on the values of the kinematic viscosity and the magnetic diffusivity, numerous different flow behaviors can be observed. As a function of the viscosity the flows can vary from a laminar to a highly turbulent state and the magnetic diffusivity allows to change the dynamics from a highly diffusive transport to an almost frozen-in advection of the magnetic field. Therefore, in the turbulent state, even in the statistically homogeneous case, a large range of dynamically active scales can be observed. Most of the interesting applications of MHD are however not statistically homogeneous due to the presence of solid walls. Examples are the planetary dynamo mechanism, magnetically confined fusion plasmas and industrial applications involving liquid metals [1,2]. In order to study these phenomena, either experiments need to be carried out, or a set of nonlinear differential equations must be solved, combined with adequately chosen boundary conditions. In most cases, these equations cannot be solved analytically, so that numerical integration is needed in order to describe the dynamics. A wide range of MHD solvers have been developed

* Corresponding author.

http://dx.doi.org/10.1016/j.jcp.2014.05.038
0021-9991/

over the last decades and an exhaustive listing is beyond the scope of this paper. Nevertheless, we will mention several approaches which are used to compute MHD in wall-bounded geometry. A review of MHD solvers developed to compute fusion-plasma-related flows is given in [3], solvers aiming at a description of dynamo computations are, for example, given in [4–6] and computations investigating the magnetorotational instability in bounded domain were reported by Rüdiger and Shalybkov [7], Gissinger et al. [8] and Willis and Barenghi [9]. An early numerical approach to study MHD in cylindrical geometry was proposed and validated by Shan et al. [10] and more recently applied to spherical geometry by Mininni et al. [11]. Most of these solvers are adapted to either a single geometry or a particular application. To change the geometry substantial effort must be invested to adapt the numerical mesh or to change the basis functions used in the numerical algorithm.

We present in this manuscript the implementation and validation of the volume-penalization method applied to magnetohydrodynamics. The strength of this approach is the high flexibility in the geometry and the ease of implementation. The volume penalization method is an immersed boundary method [12], in which both the fluid region and the confining boundaries are part of the same computational domain. The influence of the boundaries is then modeled by adding a force or drag term to the dynamical equations in the part of the domain in which the boundaries are to be present. In the volume-penalization method, for the hydrodynamic case, the solid bodies are modeled as porous media whose permeability tends to zero. This so-called Navier–Stokes/Brinkman model, where the penalization source term in the momentum equation corresponds to the Darcy drag, was first proposed by Arquis and Caltagirone [13] in the context of the natural convection flow inside a cavity with porous walls. It was then generalized to study fluid–porous wall–solid boundary systems [14]. In addition to being physically motivated, this model is mathematically justified, since Angot et al. [15] rigorously proved that the method converges to the Navier–Stokes equations combined with no-slip boundaries, when the porosity in the part of the domain corresponding to the boundaries is taken infinitesimally small. A first use of the method in combination with a pseudo-spectral Navier–Stokes solver was reported in [16]. An extensive validation of the method for three dimensional fixed and moving boundaries is reported in [17].

The strength of the combination of a pseudo-spectral Navier–Stokes solver with the penalization method is the compromise between accuracy and ease of implementation while retaining a great flexibility in the choice of the geometry of the boundaries. We have already used this method to study two-dimensional MHD [18–20] which allowed to compare square, circular and periodic boundaries using the same Cartesian grid and numerical method. In the present paper we will present a detailed validation of the method for two and three-dimensional confined HD and MHD flows.

The manuscript is organized as follows. In Sections 2 and 3, we expose the physical model and its numerical discretization. Section 4 assesses the parallel performance of our implementation. As a first validation, Section 5 presents two-dimensional kinematic and magnetic test cases together with a comparison to analytical results. Validation of the three-dimensional periodic MHD calculations is exposed in Section 6.1. Subsequently Ohmic decay is considered in Section 6.2. Sections 6.3 and 6.4 compare our three-dimensional results for 3D Taylor–Couette HD and MHD flows with those available in the literature, as further validation. Section 6.5 reports on the flow induced in a conducting fluid by the presence of an imposed helical magnetic field, and Section 6.6 demonstrates the capacity of the present method to perform simulations in complex geometries. Some conclusions are drawn in Section 7 and Appendices A–D contain some further technical details.

2. MHD equations

The media we study are isothermal, incompressible and we consider constant permeability μ, permittivity ε and conductivity σ of the material. The MHD equations for this case are the Navier–Stokes equation (including the Lorentz force) and the induction equation (that combines Ohm's law, Faraday's equation and Ampère's law). Introducing conventional normalization of the velocity by the Alfvén velocity $C_a = B_0/\sqrt{\rho\mu}$, a reference magnetic field B_0 and a conveniently chosen lengthscale L, the normalized equations read,

$$\frac{\partial \boldsymbol{u}}{\partial t} - \nu\nabla^2\boldsymbol{u} = -\nabla\Pi + \boldsymbol{u}\times\boldsymbol{\omega} + \boldsymbol{j}\times\boldsymbol{B}, \tag{1}$$

and

$$\frac{\partial \boldsymbol{B}}{\partial t} - \lambda\nabla^2\boldsymbol{B} = \nabla\times[\boldsymbol{u}\times\boldsymbol{B}], \tag{2}$$

where ν is the kinematic viscosity, λ the magnetic diffusivity ($\lambda = (\sigma\mu)^{-1}$) and $\rho = 1$ is the density. The vorticity $\boldsymbol{\omega}$ and current density $\boldsymbol{j}$ are given by

$$\boldsymbol{\omega} = \nabla\times\boldsymbol{u} \tag{3}$$

$$\boldsymbol{j} = \nabla\times\boldsymbol{B}, \tag{4}$$

and $\Pi = P + \frac{1}{2}\boldsymbol{u}^2$ is the modified pressure. The velocity field $\boldsymbol{u}$ is considered incompressible and the magnetic field $\boldsymbol{B}$ divergence free,

$$\nabla\cdot\boldsymbol{u} = 0, \tag{5}$$

$$\nabla\cdot\boldsymbol{B} = 0. \tag{6}$$

To complete the problem one needs to specify the initial and the boundary conditions corresponding to the physical system that we are interested in. In particular the boundary conditions will be discussed in more detail in the rest of this manuscript.

3. The numerical code

The penalization method was introduced into two independently developed pseudo-spectral MHD solvers, the L-code from Lyon and the M-code from Marseille. The cross-check of the results obtained by the two codes allowed a careful debugging and implementation of the method.

3.1. Pseudo-spectral discretization

A classical Fourier pseudo-spectral method is used for the spatial discretization of a cubic periodic domain Ω of size 2π [21]. The physical size of the domain can be modified rescaling the box by multiplying by L_x, L_y and L_z. Spatial derivatives are evaluated in Fourier space and multiplications are computed in physical space. In the following we denote the Fourier Transform by the symbol $\hat{}$ or $\mathcal{F}\{\ \}$. All fields are represented as truncated Fourier series and here we show this representation explicitly for the velocity:

$$\boldsymbol{u}(\boldsymbol{x},t)=\sum_{k_x=-N_x/2}^{N_x/2-1}\sum_{k_y=-N_y/2}^{N_y/2-1}\sum_{k_z=-N_z/2}^{N_z/2-1}\widehat{\boldsymbol{u}}(\boldsymbol{k},t)e^{\imath\boldsymbol{k}\cdot\boldsymbol{x}}, \tag{7}$$

$$\widehat{\boldsymbol{u}}(\boldsymbol{k},t)=\frac{8\pi^3}{N_xN_yN_z}\sum_{n_x=0}^{N_x-1}\sum_{n_y=0}^{N_y-1}\sum_{n_z=0}^{N_z-1}\boldsymbol{u}(\boldsymbol{x}_{\mathbf{n}},t)e^{-\imath\boldsymbol{k}\cdot\boldsymbol{x}_{\mathbf{n}}}, \tag{8}$$

with the wave vector $\boldsymbol{k}=(k_x,k_y,k_z)$ where $-N_x/2\le k_x\le N_x/2-1$, $-N_y/2\le k_y\le N_y/2-1$, $-N_z/2\le k_z\le N_z/2-1$, $\boldsymbol{x}_{\mathbf{n}}=(n_x2\pi/N_x,n_y2\pi/N_y,n_z2\pi/N_z)\in[0,2\pi]^3$ with $n_x=0,\ldots,N_x-1,n_y=0,\ldots,N_y-1,n_z=0,\ldots,N_z-1$. The number of grid points in x, y and z-direction, N_x, N_y and N_z, respectively, can be adapted to obtain the accuracy needed in the different directions. To avoid aliasing errors, *i.e.*, the production of small scales due to nonlinear terms which are not resolved on the grid, the velocity and magnetic fields are dealiased at each time step by truncating its Fourier coefficients using the 2/3 rule [21]. For the transformation between physical and Fourier space two different Fourier transforms were used in the two codes, firstly the P3DFFT routine in the M-code, based on the FFTW library, secondly the JMFFT library in the L-code. Both Fourier Transforms have an order of complexity of $N\log_2 N$ with $N=N_xN_yN_z$.

The pressure term can be eliminated from the equations in spectral space by using the incompressibility condition of the medium. This introduces the projector $P_{ij}=\delta_{ij}-k_ik_j/k^2$ in front of the nonlinear term. Eqs. (1) and (2) in spectral space are then written:

$$\frac{\partial\hat{u}_i}{\partial t}+\nu k^2\hat{u}_i=P_{ij}\left\{\widehat{(\boldsymbol{u}\times\boldsymbol{\omega})}+\widehat{\boldsymbol{j}\times\boldsymbol{B}})_j\right\}, \tag{9}$$

$$\frac{\partial\hat{B}_i}{\partial t}+\lambda k^2\hat{B}_i=\left[\imath\boldsymbol{k}\times\widehat{(\boldsymbol{u}\times\boldsymbol{B})}\right]_i, \tag{10}$$

where $k^2=|\boldsymbol{k}^2|$.

3.2. Penalization method

The volume penalization method is based on the idea of modeling solid bodies as porous media whose permeability tends to zero. The flow is considered in a domain in which both fluid and solid domains are embedded. The difference between the fluid and solid subdomain is the permeability. In the fluid domain the permeability is infinite and in the solid domain the permeability tends to zero. The method allows to consider an arbitrary shape and number of obstacles. The equations are modified by adding the penalization term:

$$\frac{\partial\boldsymbol{u}}{\partial t}=\boldsymbol{u}\times\boldsymbol{\omega}-\nabla\Pi+\nu\nabla^2\boldsymbol{u}+\boldsymbol{j}\times\boldsymbol{B}-\frac{\chi}{\eta}(\boldsymbol{u}-\boldsymbol{u}_{wall}) \tag{11}$$

$$\frac{\partial\boldsymbol{B}}{\partial t}=\nabla\times(\boldsymbol{u}\times\boldsymbol{B})+\lambda\nabla^2\boldsymbol{B}-\frac{\chi}{\eta}(\boldsymbol{B}-\boldsymbol{B}_{wall}), \tag{12}$$

with $\boldsymbol{u}_{wall}$ and $\boldsymbol{B}_{wall}$ the imposed values of the velocity and magnetic field in the solid domain and η is the permeability of the solid domain, *i.e.*, the penalization parameter, which could be different for each equation, and $\chi(\boldsymbol{x},t)$ the mask function (see Fig. 1):

$$\chi(\boldsymbol{x},t)=\begin{cases}0 & \text{for } \boldsymbol{x}\in\Omega_f,\ \text{the fluid domain}\\ 1 & \text{for } \boldsymbol{x}\in\Omega_s,\ \text{the solid domain.}\end{cases} \tag{13}$$

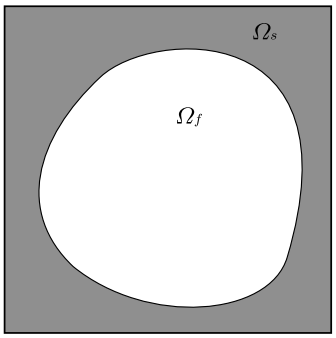

Fig. 1. The computational domain Ω contains both the fluid domain Ω_f and the solid domain Ω_s.

Note that $\boldsymbol{B}_{wall}$ can be freely chosen, we are not obliged to penalize all components. For instance choosing $\boldsymbol{B}_{wall} = \boldsymbol{B}_{\parallel}$ with $\boldsymbol{B}_{\parallel}$ the component of $\boldsymbol{B}$ parallel to the wall, only penalizes the normal component and leaves the parallel component free. According to Eqs. (11) and (12), the flow is governed by the Navier–Stokes and induction equations in Ω_f, and by Darcy's law in Ω_s for small η (for more details see Appendix A). As mentioned in the introduction, the convergence of the velocity of the penalized equation in the limit of vanishing η to the solution given by the Navier–Stokes equations with no-slip boundary conditions was rigorously proven by Angot et al. [15] for fixed obstacles. The estimates were then refined by Carbou and Fabrie [22], who demonstrated that the solution of the penalized equations converges in the L_2-norm with $\sqrt{\eta}$ towards the solution of the non-penalized equations with Dirichlet boundary conditions. Similar results are anticipated for the induction equation.

In the present investigation we focus on Dirichlet boundary conditions for both the velocity field and the magnetic field. This gives by no means an account for all possible magnetic boundary conditions. For instance, in the case of a perfect conductor surrounding the magnetofluid, only the normal component of the magnetic field is zero at the wall. The further boundary conditions involve the current density and therefore necessitate the possibility to impose Neumann boundary conditions. A first step towards the implementation of such conditions is given in Appendix C. In several applications in the presence of strong imposed magnetic fields, it is in practice enough to impose the magnetic field at the wall. For those applications the present method is directly applicable. For the situations in which the magnetic field is determined by nonlocal interactions with the exterior domain, more sophisticated methods are needed.

To use a pseudo-spectral solver we need to Fourier-transform Eqs. (11) and (12) and we obtain

$$\frac{\partial \hat{u}_i}{\partial t} + \nu k^2 \hat{u}_i = P_{ij}\left\{\left[\widehat{\boldsymbol{u}\times\boldsymbol{\omega}} + \widehat{\boldsymbol{j}\times\boldsymbol{B}} - \mathcal{F}\left\{\frac{\chi}{\eta}(\boldsymbol{u}-\boldsymbol{u}_{wall})\right\}\right]_j\right\}. \tag{14}$$

We stress here that the Riesz projector P_{ij} is also applied to the penalization term. Indeed, this form straightforwardly appears in the Fourier-transformed equations when the pressure is eliminated by solving a Poisson equation. The fact that the projector also acts on the penalization term is important to ensure incompressibility, since the penalization term is not necessarily divergence free at the fluid–solid boundary. This is also the case for the magnetic field. Due to the penalization term, the magnetic field is no longer divergence free. One way used in the L-code to cure this is to add an auxiliary pressure to the magnetic field

$$\frac{\partial \boldsymbol{B}}{\partial t} - \lambda\nabla^2\boldsymbol{B} = \nabla\times[\boldsymbol{u}\times\boldsymbol{B}] \underbrace{-\nabla\Xi}_{\substack{\text{Auxiliary}\\ \text{pressure}}} \underbrace{-\frac{\chi}{\eta}(\boldsymbol{B}-\boldsymbol{B}_{wall})}_{\text{Penalization term}}. \tag{15}$$

In the absence of boundaries in the domain, this pressure gradient would be equal to zero, as can be directly seen by solving a Poisson equation for Ξ and using the solenoidality constraint, Eq. (6). Indeed the (curl)-term $i\boldsymbol{k}\times(\widehat{\boldsymbol{u}\times\boldsymbol{B}})$ is necessarily divergence free. Eliminating the pressure from Eq. (15), we find for the Fourier-transformed equation for the magnetic field,

$$\frac{\partial \hat{B}_i}{\partial t} + \lambda k^2 \hat{B}_i = P_{ij}\left\{\left[i\boldsymbol{k}\times(\widehat{\boldsymbol{u}\times\boldsymbol{B}}) - \mathcal{F}\left\{\frac{\chi}{\eta}(\boldsymbol{B}-\boldsymbol{B}_{wall})\right\}\right]_j\right\}, \tag{16}$$

which guarantees the incompressibility.

Another way adopted in the M-code to impose the constraint $\nabla\cdot\boldsymbol{B}=0$ is the so-called Helmholtz decomposition of a vector field, *i.e.*, a decomposition into its rotational and irrotational part $\boldsymbol{B} = \nabla\times\Psi + \nabla\Phi$. Solving Eq. (12) we obtain a field $\boldsymbol{B}^*_{n+1}$ which is not divergence free because of the contribution from the penalization term. We take the divergence of $\boldsymbol{B}^*_{n+1}$ to eliminate the irrotational part and we get $\nabla\cdot\boldsymbol{B} = \nabla^2\Phi$. We solve the Poisson equation to evaluate Φ and to calculate its gradient that we subtract from $\boldsymbol{B}^*_{n+1}$. Hence we have the new divergence free magnetic field $\boldsymbol{B}_{n+1}$ with $\nabla\cdot\boldsymbol{B}_{n+1} = \nabla\cdot(\boldsymbol{B}^*_{n+1} - \nabla\Phi) = 0$.

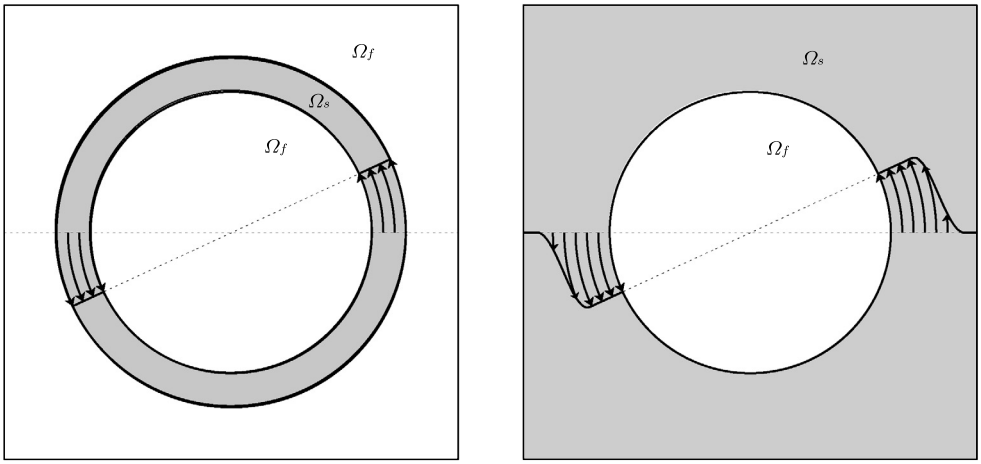

Fig. 2. Leaving a part of the domain unpenalized at the edges of the computational domain allows to use inhomogeneous Dirichlet conditions at the fluid solid interface, without violating the periodicity condition at the edge of the domain (left). Another option is to interpolate the imposed velocity to a zero value with a horizontal tangent at the domain frontier with an interpolating Hermite polynomial. The velocity field in the whole computational region belongs then to the C^1 class (right).

The penalization method allows for a simple implementation of complex geometries, since to change the shape of the walls, one only needs to redefine the mask function. This is a huge advantage, because almost no effort is required to modify the shape of the flow geometry during an investigation and arbitrarily complex shapes can be considered. Several limitations should however be mentioned. First, the dynamical equations are solved in both the fluid domain and the penalized domain, so that, if the penalized domain is large, an important part of the numerical resources is used to compute the dynamically unimportant flow inside the walls (see for example Section 6.4). Second, the present work considers the implementation of the penalization technique into a pseudospectral method. Such methods discretize the numerical domain on a Cartesian grid, and therefore it is not straightforward to use mesh refinement near solid walls. This means that if one wants to refine the mesh to capture smaller scale dynamics near boundaries, one needs to globally increase the resolution.

Intrinsically, the boundary conditions of the Fourier pseudo-spectral solver are periodic in the three directions. Thus in the computational domain this periodicity must be satisfied. This imposes certain constraints on the geometries and especially on the boundary conditions that can be considered. If in the geometry sketched in Fig. 1 the solid domain corresponds to no-slip walls, *i.e.* $\boldsymbol{u}_{wall} = 0$, the periodicity condition is met automatically. However, if the outer-walls are chosen to move in solid-body rotation anti-clockwise, the left border of the domain will move downwards whereas the right border will move upwards. In that case the periodicity condition is not satisfied. A solution to this problem is to add a third, unpenalized, subdomain outside the walls which will allow to respect the periodic boundary conditions of the computational domain. This solution is sketched in Fig. 2 (left). However it has an inconvenience which we will describe below.

Discontinuities in the velocity field, or in its gradients, are a source of Gibbs oscillations. These oscillations are an unavoidable feature in the present approach, and as long as their amplitude is small compared to physical effects, they do not constitute a serious problem in most cases and we have not encountered situations in which these oscillations were strong enough to cause numerical instabilities. When discontinuities become strong, the Gibbs-oscillations also increase in size. Considering Fig. 2 (left), it is clear that if the solid domain turns and the outer fluid domain is very small, the velocity gradient becomes strong in the outer fluid domain and the discontinuity of the velocity gradient will become large on the interface between Ω_s and the outer Ω_f. Gibbs oscillations might get strong in this case. One solution is the following. Instead of imposing in Ω_s a solid body rotation, we impose a velocity profile which gives the correct boundary condition at the solid–fluid interface, and which smoothly tends to zero towards the edges of the computational domain, Fig. 2 (right). The latter solution is slightly more complicated since an interpolation needs to be computed, using an interpolating Hermite polynomial for instance. Its advantage is that the continuity of the solution and its derivatives between the boundary value and zero value can be imposed in a smooth way, which yields an improved order of convergence of the algorithm, as we will see in Section 5 (an analytical analysis can be found in Appendix B).

Another drawback of the penalization method is that it is not yet possible to impose inhomogeneous Neumann conditions at the boundaries using a Fourier spectral code. In Appendix C a one-dimensional penalization method for taking into account non-homogeneous Neumann boundary conditions is presented. The lack of a three-dimensional implementation makes it not yet possible to impose arbitrary values of the velocity gradient or magnetic gradient, for example, to impose the vorticity and the current density at the walls. This would in particular be important to model the influence of solid boundaries with arbitrary magnetic properties on the magnetic field generated in the fluid. A recent investigation by Kadoch et al. [23] presents a technique for implementing homogeneous Neumann conditions using the penalization method with a spectral method. The extension to three-dimensional inhomogeneous Neumann conditions is an important perspective for further research.

3.3. Time-discretization

Two different implementations of the penalization method in the time-advancing scheme will be compared. The first is explicit and constrains the penalization parameter η to be bigger than the time step Δt to avoid numerical instabilities. The second is a semi-implicit implementation that allows the penalization parameter in principle to be independent of the time step. Second and third order time schemes are used. In all approaches an exact integration of the viscous and magnetic diffusion term is used. In the following two sections these different methods are detailed.

3.3.1. Explicit implementation of the penalization term

In this section we detail the time integration of the equations using an explicit treatment of the nonlinear and penalization terms. It must be noted that along with its simplicity and robustness this approach has a drawback: the explicit treatment of the penalization term imposes a stability condition, in addition to the usual CFL condition. An analytical analysis of the magnetic part of the method has yet to be done to check if it adds another stability condition. Up to now no problem occurred if the same stability criteria were used for the velocity and the magnetic field.

The basic time-stepping schemes that are implemented are an adaptive second and third order Adams–Bashforth method (denoted by AB2 and AB3 respectively). The use of these schemes fits well into our general concept of compromise between the ease of implementation and computational efficiency. Exact integration of the diffusion term is feasible because the Laplace operator is diagonal in Fourier space and hence no linear system has to be solved. It improves stability of the scheme, avoiding the stability condition $\Delta t < \Delta x^2/\nu$. The remaining terms are discretized explicitly to avoid the solution of nonlinear equations, however it implies a CFL condition on the time step size Δt and also a condition due to the explicit discretization of the penalization term, *i.e.*, $\Delta t < \eta$ for AB2 and $\Delta t < \frac{6}{11}\eta$ for AB3, as linear stability analysis shows [17].

For illustration, the equations will be given for the case of the velocity only. The discretization of the magnetic field is handled analogously, the only difference is the exact form of the nonlinear and penalization terms. First the Navier–Stokes equation is rewritten in the form of a nonlinear evolution equation and transformed into Fourier space,

$$\partial_t \boldsymbol{u} - \nu\nabla^2\boldsymbol{u} = N(\boldsymbol{u}) \tag{17}$$

$$\partial_t \widehat{\boldsymbol{u}} + \nu k^2 \widehat{\boldsymbol{u}} = \widehat{N}(\widehat{\boldsymbol{u}}). \tag{18}$$

For the initial condition $\widehat{\boldsymbol{u}}(\boldsymbol{k}, t_n)$, the above equation has the following solution

$$\widehat{\boldsymbol{u}}(\boldsymbol{k}, t_{n+1}) = e^{-\nu\Delta t_{n+1}k^2}\widehat{\boldsymbol{u}}(\boldsymbol{k}, t_n) + \int_{t_n}^{t_{n+1}} e^{-\nu(t_{n+1}-s)k^2}\widehat{N}\big(\widehat{\boldsymbol{u}}(\boldsymbol{k}, s)\big)ds, \tag{19}$$

which can be discretized

$$\text{AB2} \quad \longrightarrow \quad \widehat{\boldsymbol{u}}(\boldsymbol{k}, t_{n+1}) = e^{-\nu\Delta t_{n+1}k^2}\big(\widehat{\boldsymbol{u}}(\boldsymbol{k}, t_n) + \beta_{10}\widehat{N}^n + \beta_{11}e^{-\nu\Delta t_n k^2}\widehat{N}^{n-1}\big) \tag{20}$$

$$\text{AB3} \quad \longrightarrow \quad \widehat{\boldsymbol{u}}(\boldsymbol{k}, t_{n+1}) = e^{-\nu\Delta t_{n+1}k^2}\big(\widehat{\boldsymbol{u}}(\boldsymbol{k}, t_n) + \beta_{20}\widehat{N}^n + e^{-\nu\Delta t_n k^2}\big(\beta_{21}\widehat{N}^{n-1} + \beta_{22}e^{-\nu\Delta t_{n-1}k^2}\widehat{N}^{n-2}\big)\big), \tag{21}$$

with $\widehat{N}^n$ denoting the value of the nonlinear term at the time instant t_n, the second order Adams–Bashforth coefficients

$$\begin{aligned}
\beta_{10} &= \frac{1}{2}\frac{\Delta t_{n+1}}{\Delta t_n}(\Delta t_{n+1} + 2\Delta t_n)\\
\beta_{11} &= -\frac{1}{2}\frac{\Delta t_{n+1}^2}{\Delta t_n},
\end{aligned} \tag{22}$$

and the third order Adams–Bashforth coefficients

$$\begin{aligned}
\beta_{20} &= \frac{\Delta t_{n+1}(2\Delta t_{n+1}^2 + 6\Delta t_n\Delta t_{n+1} + 3\Delta t_{n-1}\Delta t_{n+1} + 6\Delta t_n^2 + 6\Delta t_{n-1}\Delta t_n)}{6\Delta t_n(\Delta t_n + \Delta t_{n-1})}\\
\beta_{21} &= \frac{-\Delta t_{n+1}^2(2\Delta t_{n+1} + 3\Delta t_n + 3\Delta t_{n-1})}{6\Delta t_{n-1}\Delta t_n}\\
\beta_{22} &= \frac{\Delta t_{n+1}^2(2\Delta t_{n+1} + 3\Delta t_n)}{6\Delta t_{n-1}(\Delta t_n + \Delta t_{n-1})},
\end{aligned} \tag{23}$$

where $\Delta t_n = t_n - t_{n-1}$ [16]. For start-up a first order scheme is used, as two time steps are required to start a second-order scheme. Similarly a first order scheme and a second order scheme are used to start the third order scheme.

The time step size control is based on the CFL stability limit of the explicit discretization of the nonlinear term, with addition of the stability criterion due to the penalization. Therefore, at each time step t_n, the maximal point-wise velocity is computed and the new time step is given by $\Delta t_{n+1} = C\Delta x/U_{max}$ where $C < 1$ is the CFL constant and Δx is the minimal spatial grid size. Moreover, the time step has to verify the condition $\Delta t_{n+1} < \eta$ (AB2) or $\Delta t_{n+1} < \frac{6}{11}\eta$ (AB3) due to the presence of the penalization term. The same method is applied to the magnetic field and the time step is chosen to be small enough to verify the stability criteria of both the magnetic field and velocity field discretization.

Table 1
Summary of the elapsed physical time during simulations for different resolutions and number of processors.

Processors	1024	2048	4096	8192
Resolution 512^3 (s)	106	52	28	14
Resolution 1024^3 (s)	877	438	212	105

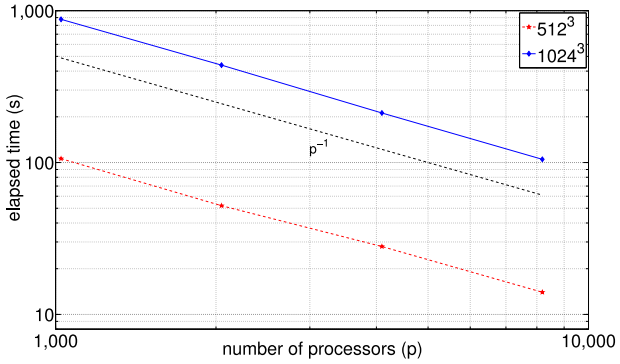

Fig. 3. Parallel scaling on Turing for 512^3 and 1024^3 on [1024, 2048, 4096, 8192] processors.

3.3.2. Semi-implicit implementation

As noted in the previous section, the stability condition for a third order time scheme constrains $\Delta t < \frac{6}{11}\eta$. To avoid this limitation, an implicit implementation was introduced by Kolomenskiy and Schneider [17] for Burgers' equation and extended to Navier–Stokes' equation by Jause-Labert et al. [24]. In this case the penalization term is evaluated at the time step t_{n+1}. The penalization is thus no longer treated together with the nonlinear term. The diffusion term, as in the explicit method, is exactly integrated.

This method is more time-expensive because two additional Fourier transforms are required. In addition to the projection of the nonlinear term, a second projection is realized (that includes the penalization term at t_{n+1}) to ensure the solenoidal nature of the two considered fields. The fact that the time step can be adaptive (taking into account the CFL condition) makes this technique more suitable for unsteady simulations. The penalization term is introduced using a first order time scheme, which does not influence negatively the precision as long as boundaries are fixed.

The magnetic equations being handled analogously we present the new time scheme for the velocity field

$$\hat{u}_i(\boldsymbol{k}, t_{n+1}) = P_{ij}\left\{\mathcal{F}\left[\frac{\mathcal{F}^{-1}\{\mathcal{Q}_i^n\} + \frac{\Delta t}{\eta}\chi\, u_{wall_i}(\boldsymbol{x}, t_{n+1})}{1 + \frac{\Delta t}{\eta}\chi}\right]_j\right\}. \tag{24}$$

The third order Adam–Bashforth scheme is retained for the nonlinear terms in this formulation

$$\mathcal{Q}_i^n = e^{-\nu\Delta t_{n+1}k^2}\left(\widehat{\boldsymbol{u}}(\boldsymbol{k}, t_n) + \beta_{20}\widehat{N}^n + e^{-\nu\Delta t_n k^2}\left(\beta_{21}\widehat{N}^{n-1} + \beta_{22}e^{-\nu\Delta t_{n-1}k^2}\widehat{N}^{n-2}\right)\right). \tag{25}$$

This numerical scheme for a penalization parameter η being sufficiently small ($\eta \ll \Delta t$) converges towards an explicit modified scheme where the time step Δt replaces the penalization parameter η and where the nonlinear term vanishes in the solid region. We therefore call this method *semi-implicit*. This is further explained in Appendix D. For this case with very small penalization parameter, the permeability of the solid media is given by the value of the time step. The asymptotic convergence of the porous boundaries towards a solid wall, if η is sufficiently small, is in that case limited by the value $\eta_{\text{effective}} \approx \Delta t$.

4. Parallel performance

The parallelization of the M- and L-codes is based on P3DFFT (based itself on the parallelized FFTW) or JMFFT respectively, and uses MPI libraries. In order to establish the scalability of the numerical method as a function of the number of processors, simulations for 100 time-steps of an MHD problem for different grid resolutions were performed on the *Turing* calculator of the French high performance computing center IDRIS, with the M-code. The results are summarized in Table 1 and in Fig. 3.

The code fits very well the p^{-1} scaling law (dashed line), p being the number of processors (and thus processes) used. It was expected since our libraries yield that same scaling law.

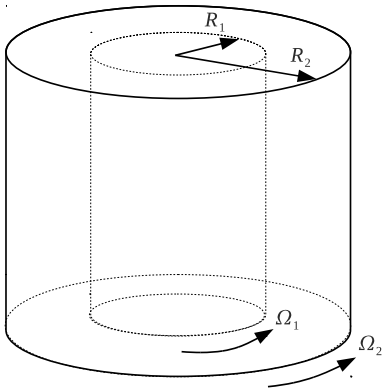

Fig. 4. Taylor–Couette flow configuration.

5. Two-dimensional validation

In this section we present a purely HD test-case, the two-dimensional Taylor–Couette flow and a purely magnetic test-case, the z-pinch configuration. For both cases analytical solutions are known, which allows a careful convergence study and which allows to check different ways to introduce the boundary conditions.

5.1. Two-dimensional Taylor–Couette flow

We consider the classical two-dimensional HD problem of a flow between two coaxial rotating cylinders (*e.g.*, Taylor [25]). The inner cylinder rotates at constant speed, while the outer cylinder is kept at rest. The steady flow solution of the problem is

$$U_\theta(r) = \frac{\Omega_2 R_2^2 - \Omega_1 R_1^2}{R_2^2 - R_1^2} r + \frac{(\Omega_1 - \Omega_2) R_1^2 R_2^2}{R_2^2 - R_1^2} \frac{1}{r}, \tag{26}$$

where $\Omega_{(1,2)}$ are the angular velocities of the cylinders, $R_{(1,2)}$ the radii of the cylinders and r the cylindrical coordinate (see Fig. 4).

The relative L_2 error in the fluid domain $\| f_{numerical} - f_{analytical} \|_{L_2} / \| f_{analytical} \|_{L_2}$ with f being the considered field, is calculated for different penalization parameters η and number of grid points N, in one direction with $N = N_x = N_y$ and $N_z = 4$.

As mentioned above, the present calculation is entirely HD. The simulations are carried out until a steady state is obtained, so that the error is independent of the time discretization. A cubic domain with size-length 2π is considered, the time step is fixed to a value $\Delta t = 5 \cdot 10^{-5}$ and the kinematic viscosity $\nu = 1$. The radii R_1, R_2 are $(0.32\pi, 0.82\pi)$ respectively. At $t = 0$ the fluid domain is at rest and the inner-cylinder is set into movement with a fixed velocity $U_\theta(R_1) = 1$ while the velocity $U_\theta(R_2)$ is kept equal to zero. The runs are stopped when the time $t_{max} = 5$ is reached. At this time instant, the difference in the kinetic energy between two iterations is less than 10^{-9} (for a kinetic energy of order unity), which indicates that a steady state is satisfactorily achieved.

The velocity profile imposed in the mask is chosen in two different ways, corresponding to the discussion in Section 3.2. In the first case, the velocity in the inner cylinder is straightforwardly set to a solid-body rotation, $U_\theta = \Omega_1 r$, in the inner cylinder and $U_\theta = 0$ in the outer cylinder. This is the most obvious choice. The component U_r is set to zero at the boundaries. The velocity field is hereby continuous, but there exists a discontinuity of the velocity field derivative at the fluid boundaries (which is also the case in the real, physical situation). The error evolution with the penalization parameter and the convergence of the error with the resolution are shown in Figs. 5 and 6. For these calculations the expected $\sqrt{\eta}$ convergence order [22] is found and the convergence is second order in space as a function of the resolution N, confirming the results in [17]. We also observe a saturation of the error for large N, corresponding to the penalization error.

A second way to impose the velocity in the mask will now be described. In this particular test-case the analytical solution is known (Eq. (26)) and we can use this information to increase the precision of the method. As mentioned in Section 3.2, Gibbs oscillations are created due to discontinuities in the fluid variables or their derivatives. The discontinuity in the velocity gradient field can here be removed by using a 4th order Hermite interpolation at the boundaries at $r = R_1, R_2$. Any purely azimuthal, axisymmetric flow is solenoidal so we can freely choose the velocity $U_\theta(r)$ in the mask, as long as it respects the correct boundary conditions at $r = R_1$, $r = R_2$ and $r = \pi$, the latter condition being imposed by the periodicity of the pseudo-spectral method. The velocity $U_\theta(r)$ in the mask is chosen such that velocity and derivative at the fluid–solid boundaries are continuous. Subsequently the velocity field is interpolated to decay smoothly from the analytical solution at $r = R_1, R_2$ to zero at $r = 0$ and $r = \pi$ respectively, using an interpolating Hermite polynomial. Any discontinuity on the derivative of the velocity field at the fluid boundaries is thus avoided and the Gibbs oscillations are hereby significantly

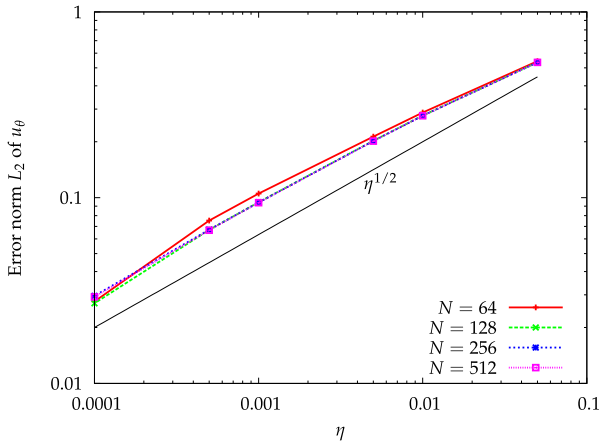

Fig. 5. Taylor–Couette: convergence of the relative L_2 error of u_θ with the penalization parameter η, convergence order $\sqrt{\eta}$.

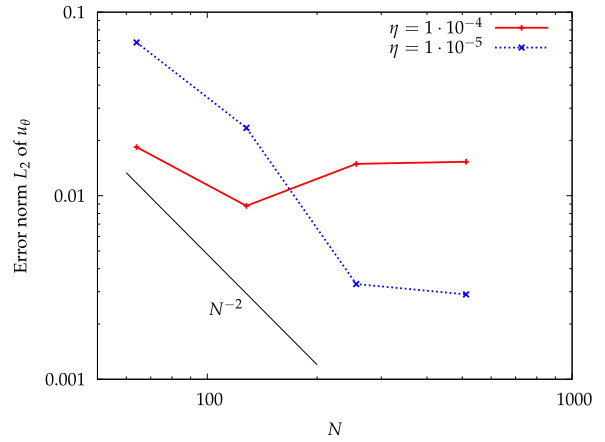

Fig. 6. Taylor–Couette: convergence of the relative L_2 error of u_θ with the resolution N which shows a second order convergence.

reduced. In principle even higher order velocity derivatives could be smoothed in this way using higher order Hermite interpolation. Note that a similar regularization is used in [26] for the velocity field, where the imposed velocity in the mask is called an internal flow.

The error as a function of the penalization parameter and the convergence of the error with the resolution are shown respectively in Figs. 7 and 8. The numerical error is only calculated in the fluid domain. It is observed that the convergence of the error with the penalization parameter is close to third order. An optimum for the penalization parameter depending on the resolution appears, when the gridscale becomes of order $\sqrt{\nu\eta}$. At this scale the viscous term becomes of the order of the penalization term. In Figs. 7 and 8 results for both explicit and semi-implicit methods are presented.

The regularization of the boundary conditions using an interpolation clearly improves the numerical convergence of the solution with the penalization parameter. Also the convergence with the grid resolution is improved. If the Hermite interpolation is used, a fourth order convergence with N is found for both the explicit (dashed line) and semi-implicit (solid line) implementations (see Fig. 8). We recall that if no regularization of the velocity field is introduced, second order convergence is recovered (see Fig. 6).

5.2. The z-pinch

The second validation test is the reproduction of the z-pinch phenomenon, a well-known textbook example of a confined plasma situation [27]. This configuration is illustrated in Fig. 9. Two ideal electrodes drive an axial current in the z-direction producing a purely azimuthal magnetic field (in the θ-direction). The current density in the z-direction, which together with the induced azimuthal magnetic field yield a radially pinching Lorentz force, is the motivation for the name z-pinch. In this configuration we set the velocity to zero so the code is entirely magnetic. We impose the boundary conditions $B_\theta = B_C$ and $B_r = 0$ at $r = R_1$ the radius of the fluid domain. The component B_z is not penalized and can freely evolve.

Periodic conditions are set in the axial direction. In this configuration the governing equations reduce to

$$\partial_t \boldsymbol{B} = \lambda \nabla^2 \boldsymbol{B} \tag{27}$$

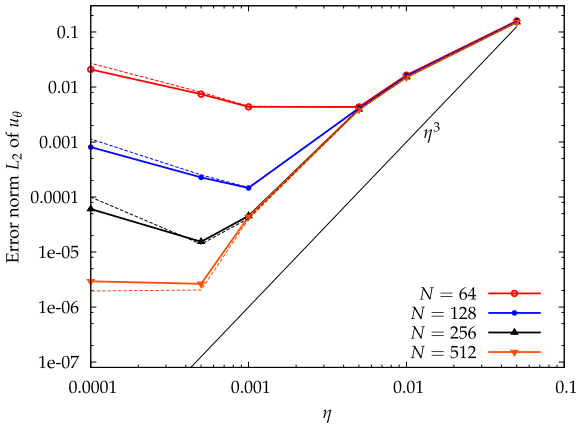

Fig. 7. Taylor–Couette: convergence of the relative L_2 error with the penalization parameter η, semi-implicit (solid line) and explicit (dashed line) methods.

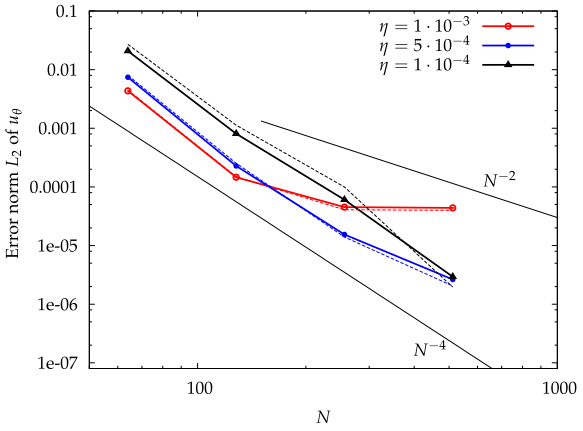

Fig. 8. Taylor–Couette: convergence of the relative L_2 error with the resolution N, semi-implicit (solid line) and explicit (dashed line) methods.

In cylindrical coordinates, the steady state solution is a linear evolution of the azimuthal magnetic field

$$B_\theta(r) = \frac{B_C r}{R_1}. \tag{28}$$

The quantity B_C/R_1 is linked to the constant axial current density, using Ampère's law,

$$j_z = \frac{2B_C}{R_1}. \tag{29}$$

The computational domain is chosen similar to Fig. 2 (left). The mask is chosen to be annular, leaving the outer domain free to adapt to the periodic boundary conditions of the computational domain. If a uniform azimuthal magnetic field is imposed inside the mask, the discontinuity in the profile of the radial derivative of the azimuthal magnetic field at the boundary causes Gibbs' oscillations in the current density, analogously to what was observed in the Taylor–Couette case. To avoid this, a linear profile of $B_\theta(r) = \frac{B_C r}{R_1}$ is imposed inside the mask to ensure a continuity with the analytical solution. This feature eliminates the discontinuity at $r = R_1$ in the derivative of the magnetic field and thus greatly reduces the oscillations for j_z. The convergence of the method can be further enhanced by using a Hermite polynomial to smoothly interpolate the magnetic field in the mask to zero at the outer boundaries of the computational domain. With this method, the continuity of the derivative of the magnetic field is assured through the entire domain (see Fig. 2 (right)).

For these simulations the number of grid points are the same as for the Taylor–Couette case ($N \in \{64, 128, 256, 512\}$). The parameters are a cubic domain with size-length 2π with magnetic diffusivity $\lambda = 1$, the time step is fixed to $\Delta t = 5 \cdot 10^{-5}$ and $t_{max} = 5$. For $t = t_{max}$ the difference in the magnetic energy between two iterations is less than 10^{-9} so we have reached the steady state. The inner radius of the annulus is $R_1 = 0.65\pi$ and the outer radius is $R_2 = 0.78\pi$. If the Hermite polynomial is used, the radius where it reaches the value 0 is $R_3 = 0.94\pi$. The boundary condition is $B_C = 1$.

In Fig. 10 the convergence of the method is shown as a function of the penalization parameter η and the resolution N. An improved convergence, proportional to η^4 or N^{-4} is observed. The relative importance of the smoothing of the magnetic field in the mask is illustrated in Fig. 10 where the results of these computations with and without regularization are

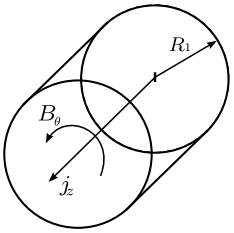

Fig. 9. z-pinch configuration.

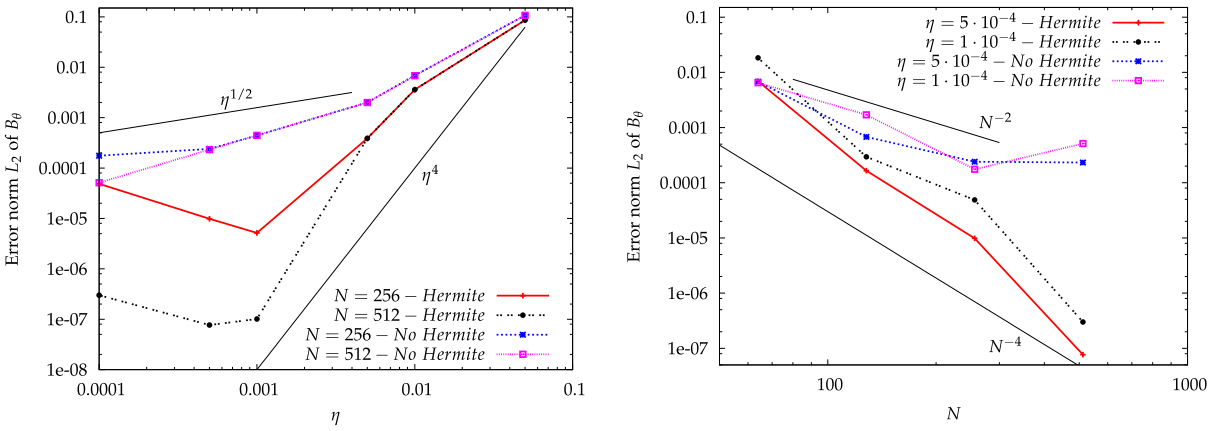

Fig. 10. z-pinch: convergence of the relative L_2 error with the penalization parameter η (left) and with the resolution N (right) for the magnetic field in the z-pinch geometry. Comparison of the results with and without Hermite polynomial interpolation.

compared. Without the regularization technique, the convergence reduces to second order in N and order $\sqrt{\eta}$ for the penalization parameter.

5.3. Assessment of the regularization method to enhance the performance of the penalization method

For these two-dimensional test cases, either Taylor–Couette or z-pinch, the error of convergence as a function of the penalization parameter and the resolution are determined. The regularization of the different fields in the solid domain (or mask) allows an enhancement of the accuracy of the numerical solution in the fluid region. The fact that the continuity of the velocity derivative field inside the solid domain affects the error inside the fluid domain is an intrinsic feature of the pseudo-spectral method. Such methods use periodic trial functions and the Gibbs oscillations introduced in one point of the domain decay only inversely proportional to the distance from the discontinuity. The Hermite interpolation method regularizes and yields fields which are C^1 in the whole domain (see Appendix B for an analytical analysis of the Hermite regularization). Gibbs oscillations are thus reduced and consequently the numerical errors are also decreased considerably. The limitation of this method is that an analytical solution must be known, or a baseflow, which is not far from the expected developed flow. Without such regularization the convergence is reduced to second order in resolution, which can be sufficient for many applications, as illustrated in the following sections.

6. Three-dimensional validation

In this section the code will be validated by considering three-dimensional test-cases. First a periodic MHD case is considered, without using the penalization method, subsequently the magnetic part of the code is validated by studying the Ohmic decay in a cylindrical cavity. Then the three-dimensional Taylor–Couette flow is studied with and without the presence of a magnetic field and to conclude we investigate the instabilities in a cylinder with helical magnetic boundary conditions.

6.1. Periodic MHD validation

To validate the capacity of the numerical code to simulate the three-dimensional nonlinear MHD equations, we reproduce first a classical test-case with periodic boundary conditions. This case is the generalization of the Orszag–Tang vortex to three dimensions. The results are compared with those of Mininni et al. [28].

The initial condition used for the simulation is given analytically and yields:

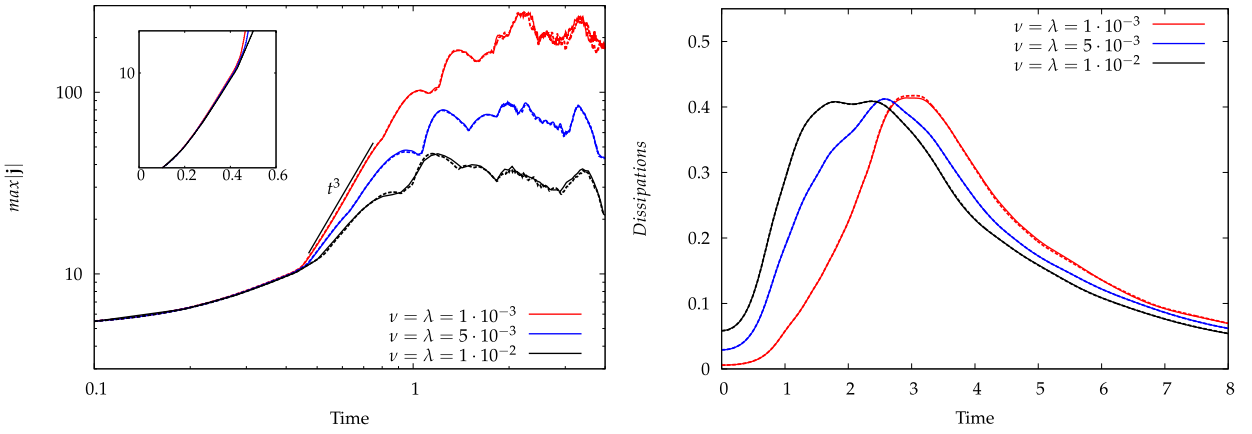

Fig. 11. Comparison of the solution of the numerical code for the time evolution of the maximum of the current (left) and total dissipation rate (right) using second (dashed line) and third order time-schemes (solid line). The inset (left) shows the evolution at early times in log-lin units.

$$\boldsymbol{u}(x, y, z, t = 0) = \left[-2\sin(y), 2\sin(x), 0\right] \quad \text{for } x, y, z \in [0, 2\pi]^3 \tag{30}$$

and

$$\boldsymbol{B}(x, y, z, t = 0) = \beta\left[-2\sin(2y) + \sin(z), 2\sin(x) + \sin(z), \sin(x) + \sin(y)\right] \tag{31}$$

with $\beta = 0.8$, the initial kinetic energy, $E_k = 2$, and the corresponding magnetic energy, $E_m = 1.92$. The energies are evaluated by $E_k = \frac{1}{2}\langle \mathbf{u}^2 \rangle$ and $E_m = \frac{1}{2}\langle \mathbf{B}^2 \rangle$ with $\langle .. \rangle$ the volume average. The maximum of the current density is calculated by

$$\max|\boldsymbol{j}| = \max\sqrt{j_x^2 + j_y^2 + j_z^2} \tag{32}$$

and the total dissipation rate is

$$\varepsilon(t) = \nu \left\langle \omega^2 \right\rangle + \lambda \left\langle j^2 \right\rangle, \tag{33}$$

where ν and λ are respectively the kinematic viscosity and the magnetic diffusivity. Three runs are performed: the first with $N^3 = 64^3$ and $\nu = \lambda = 0.01$, the second with $N^3 = 128^3$ and $\nu = \lambda = 0.005$ and the third $N^3 = 256^3$ with $\nu = \lambda = 0.001$.

The evolution of the maximum of the current density and total dissipation rate in the domain are shown in Fig. 11. Results are compared using a second- and third-order Adams–Bashforth time advancing scheme described in Section 3.3. Both schemes give the same results. The results agree well with the computations presented in Ref. [28]. The same exponential growth followed by a self similar growth $\sim t^3$ is found in our calculations for the evolution of the maximum current density (see Fig. 11 (left)). With an increasing Reynolds number *Re* the maximum of $|\boldsymbol{j}|$ is also found to be reached at later times. The evolution of the total dissipation rate (see Fig. 11 (right)) shows the same delay in the onset of the formation of small scales with increasing *Re* as exposed in the cited article. This test allows us to evaluate the full MHD code and validate the numerical results for relatively high Reynolds numbers (up to $Re = 3000$).

6.2. Ohmic decay in a periodic cylinder

In this test case we compute the evolution of the magnetic field in a periodic three dimensional cylinder imposing Dirichlet boundary conditions [29,30]. In the induction equation we set the velocity to zero so the equation for the magnetic field reduces to the diffusion equation:

$$\frac{\partial \boldsymbol{B}}{\partial t} = \nabla^2 \boldsymbol{B}. \tag{34}$$

We consider an axisymmetric case, z-independent and the magnetic field has no r component. This case is not completely three-dimensional since we use the three components of the magnetic field (B_x, B_y, B_z), but the derivatives are zero in the z direction. In cylindrical coordinates the set of equations is:

$$\begin{cases} \dfrac{\partial B_\theta}{\partial t} = \dfrac{\partial^2 B_\theta}{\partial r^2} + \dfrac{1}{r}\dfrac{\partial B_\theta}{\partial r} - \dfrac{B_\theta}{r^2} \\ \dfrac{\partial B_z}{\partial t} = \dfrac{\partial^2 B_z}{\partial r^2} + \dfrac{1}{r}\dfrac{\partial B_z}{\partial r}. \end{cases} \tag{35}$$

Using separable elementary solutions, the magnetic field can be written in the following form:

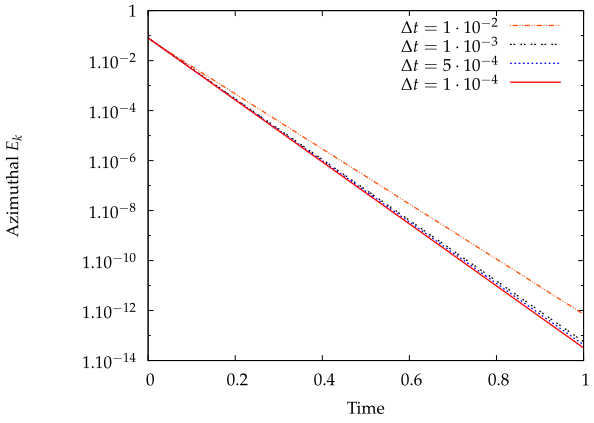

Fig. 12. Azimuthal magnetic energy decay for different time steps in a periodic cylinder.

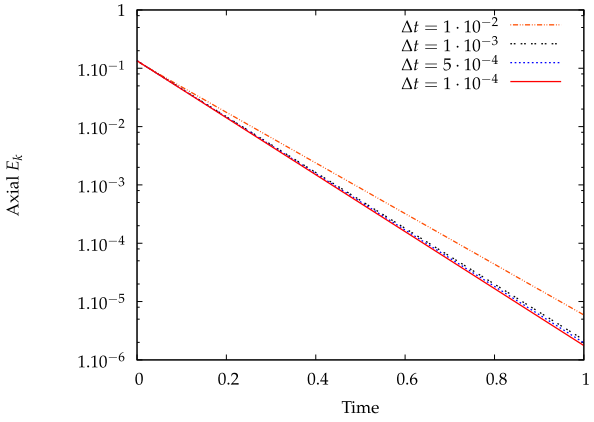

Fig. 13. Axial magnetic energy decay for different time steps in a periodic cylinder.

$$\begin{cases} B_\theta(r,t) = Af(r)e^{-\omega_\theta^2 t} \\ B_z(r,t) = Bg(r)e^{-\omega_z^2 t}. \end{cases} \tag{36}$$

Introducing the following change of parameter: $s = \omega r$ the system of equations writes:

$$\begin{cases} s_\theta^2 f'' + s_\theta f' + (s_\theta^2 - 1) f = 0 \\ s_z^2 g'' + s_z g' + s_z^2 g = 0. \end{cases} \tag{37}$$

The solutions of these equations are Bessel functions. At the radius R_0 of the cylinder the azimuthal and axial fields are set to zero. Therefore the general solution is:

$$\begin{cases} B_\theta(r,t) = J_1\left(\dfrac{j_1}{R_0} r\right) e^{-(\frac{j_1}{R_0})^2 t} \\ B_z(r,t) = J_0\left(\dfrac{j_0}{R_0} r\right) e^{-(\frac{j_0}{R_0})^2 t}. \end{cases} \tag{38}$$

Here $j_0 = 2.4048\ldots$ and $j_1 = 3.8314\ldots$ are the first zeros of the Bessel functions J_0 and J_1 respectively. The initial condition is $B_\theta(r,0) = J_1(\frac{j_1}{R_0} r)$ and $B_z(r,0) = J_0(\frac{j_0}{R_0} r)$.

In our simulation we set $R_0 = 1$. The decay rate is determined doing a least square fitting of the azimuthal and axial magnetic energy time evolutions (Figs. 12 and 13). In Table 2 we present our results for the decay rate of the azimuthal and axial fields and we compare them to the analytical values (see Eq. (38)). All the simulations are done with 96^3 grid points, the penalization parameter $\eta = 5 \cdot 10^{-4}$ and the computational domain size is $L_x = L_y = L_z = 2\pi$. We calculate the error for different fixed time steps. In none of these calculations the regularization of the magnetic field in the solid region (mask) is used.

Table 2
Comparison of analytical (see Eq. (38)) and numerical calculation of the decay rate for the Ohmic diffusion in an infinite cylinder.

Time step	Theory ω_θ^2	Numerical ω_θ^2	Error ω_θ^2	Theory ω_z^2	Numerical ω_z^2	Error ω_z^2
$1\cdot10^{-2}$	14.68	12.68	14%	5.78	4.99	14%
$1\cdot10^{-3}$		13.99	5%		5.51	5%
$5\cdot10^{-4}$		14.13	4%		5.57	4%
$1\cdot10^{-4}$		14.28	3%		5.62	3%

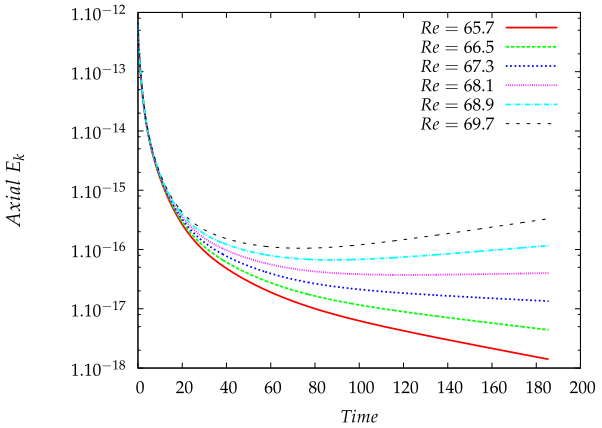

Fig. 14. Evolution of the axial kinetic energy for different *Re* numbers.

For these calculations of the diffusion of a magnetic field in a periodic cylinder the decay rate of the azimuthal and axial component of the magnetic field agree quite well with the analytical values. We find the same relative error in the azimuthal and in the axial direction at each considered time discretization.

This test-case yields a validation of the magnetic part of the numerical code and shows that the magnetic boundary conditions are well taken into account via the penalization method. Also we note that the time scheme is well implemented as it allows to recover the analytical decay rates for the considered components of the magnetic field with good accuracy. The numerical solution converges towards the analytical solution if the time step is decreased.

6.3. Three-dimensional Taylor–Couette flow

In this test case we aim to determine the critical Reynolds number for the first instability of the Taylor–Couette flow with periodic boundaries in the axial direction. Different values of the Reynolds number are explored with several calculations with a resolution of 128^3 grid-points, the penalization parameter $\eta = 5\cdot10^{-4}$ and the computational domain size is $L_x = L_y = 5\pi/2$ and $L_z = 2\pi$. To assess the influence of the Hermite interpolation method, in one of these calculations the regularization of the velocity in the solid region (mask) is used (for the case with $Re = 120$). The reference length scale is the gap between the inner and outer cylinder $\mathcal{L} = R_{ext} - R_{int}$ and the reference velocity is the inner rotation speed $U = \Omega_{int} R_{int}$. The outer cylinder is fixed. We define the Reynolds number and also a radius ratio ζ and an aspect ratio Γ as follows:

$$Re = \frac{U\mathcal{L}}{\nu}, \qquad \zeta = \frac{R_{int}}{R_{ext}}, \qquad \Gamma = \frac{L_z}{\mathcal{L}}, \tag{39}$$

where L_z is the axial length. To be able to compare with the literature we take the same values as in [31] for the dimensionless values, radius ratio and aspect ratio, $\zeta = 0.5$ and $\Gamma = 4$. The base flow consists of an azimuthal velocity only, as in the two-dimensional case (Section 5.1). The first Taylor–Couette instability is centrifugal and is characterized by vortices that appear and break the axial invariance. Velocities in the radial and axial directions thereby appear. To determine the critical Reynolds number we analyze the evolution of the axial kinetic energy. The analysis of the evolution of the axial kinetic energy allows us to assess the critical Reynolds number (when the instability is triggered). The value of the critical Reynolds is compared with a theoretical value of $Re = 68.23$ that has been determined by Chandrasekhar [32]. We present in Fig. 14 the axial kinetic energy evolution for Reynolds numbers varying from $Re = 65.7$ to $Re = 69.7$. We start the simulations with a small random perturbation so the initial axial kinetic energy is non-zero. The axial energy either grows or decays exponentially. The critical Reynolds number can be determined from Fig. 14. Increasing the Reynolds number from $Re = 67.3$ to $Re = 68.1$ the axial kinetic energy changes from decaying to increasing. A simple linear interpolation of the growth and decay rates (that are determined with a least square method fitting) gives the value of the critical Reynolds $Re_c \approx 67.9$. The estimated error compared with the theoretical result is $\sim$0.44%. The theoretical estimate is thus well approached by our numerical simulations.

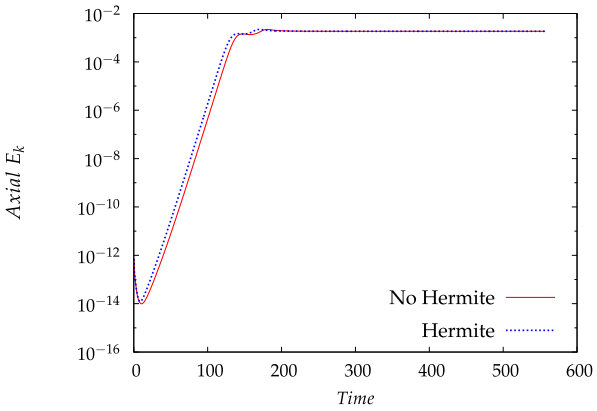

Fig. 15. Evolution of the axial kinetic energy for $Re = 120$, with and without the regularization technique.

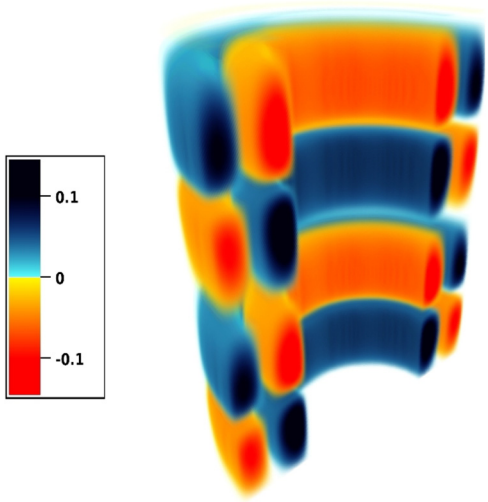

Fig. 16. Axial velocity u_z (color) for $Re = 120$. (For interpretation of colors in this figure, the reader is referred to the web version of this article.)

The Taylor vortices appear early in the simulation and they grow or decay in strength depending on the Reynolds number. Fig. 15 presents the axial kinetic energy evolution of a Taylor–Couette flow for $Re = 120$ comparing two simulations, one with Hermite regularization and one without. The difference between the two considered methods is the onset of the instability, which occurs slightly earlier if the Hermite regularization is used. Nevertheless the growth rates are similar and, when the nonlinear saturation is reached, a steady state is obtained that almost coincides for both methods. In Figs. 16 to 19 we visualize the Taylor vortices in the steady state. Two pairs of counter-rotating vortices appear. The aspect ratio is $\Gamma = 4$ so that four vortices form. In Fig. 17 we distinguish the boundary layer, in which the azimuthal vorticity is contrary to the vorticity of the Taylor-vortices. The above results have been obtained with the L-code. Those of the M-code are almost identical and are therefore not shown.

The flow structure of Figs. 16 to 19 can be compared with the one presented by Guermond et al. (Fig. 5 in [31]). The same flow topology with four vortices is found. In Figs. 18 and 19 we note that there is a transport of azimuthal momentum by the radial flow. The azimuthal velocity isosurfaces are not axial invariant but they are dragged in- and outwards by the radial flow. A positive radial velocity increases the azimuthal velocity near the inner cylinder.

To compare quantitatively both simulations, in Table 3 the maxima of the three velocity components at the steady state are compared with those of Guermond et al. [31].

The azimuthal velocity is not exactly unity because with the penalization method the precise value at the boundary is not necessarily coinciding with the numerical grid as is the case in [31]. Nevertheless the numerical method yields good agreement for all three components of the velocity with the results of the code described in [31]. The three numerical methods yield similar relative variations, and there is an improvement in the error with the regularization for the radial component of the velocity field. The improvement is limited because the tangent imposed with the Hermite polynomial is calculated using the analytical base flow, which is known in this case. Since the development of the instability makes the flow change, discontinuities appear at the fluid–solid interface and the Gibbs oscillations can grow. The improvement can be substantial if the saturated state is not far from the calculated analytical base flow.

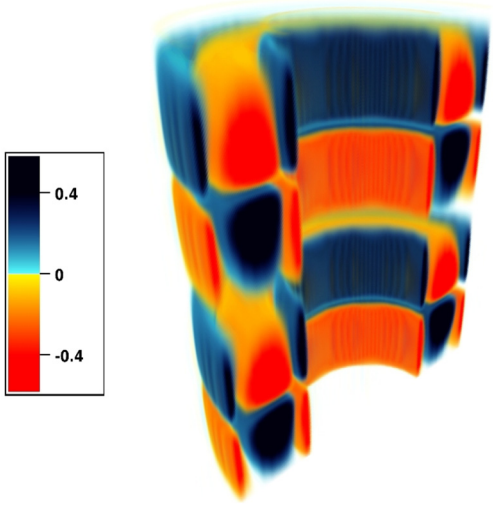

Fig. 17. Azimuthal vorticity ω_θ (color) for $Re = 120$. (For interpretation of colors in this figure, the reader is referred to the web version of this article.)

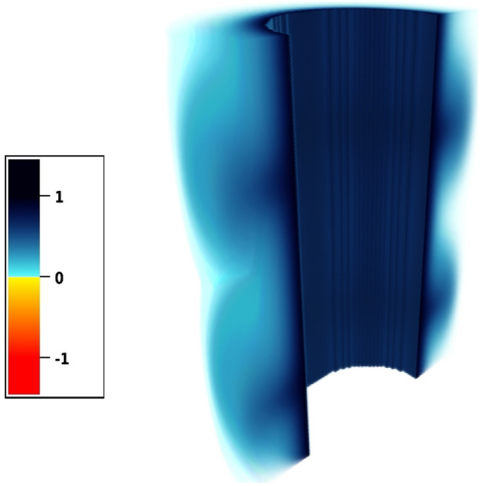

Fig. 18. Azimuthal velocity u_θ (color) for $Re = 120$. (For interpretation of colors in this figure, the reader is referred to the web version of this article.)

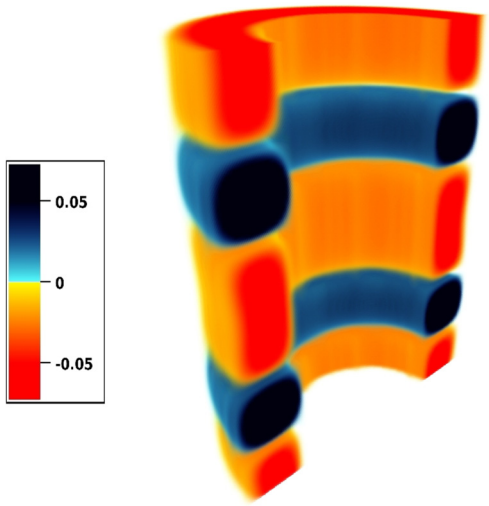

Fig. 19. Radial velocity u_r (color) for $Re = 120$. (For interpretation of colors in this figure, the reader is referred to the web version of this article.)

Table 3
Maximum velocity components comparison and relative errors for $Re = 120$ in a periodic cylinder.

	Guermond et al. [31]	3rd order semi-implicit no regularization	2nd order explicit no regularization	3rd order semi-implicit with regularization
max u_r	0.1935	0.19434 (∼0.43%)	0.1969 (∼1.75%)	0.19355 (∼0.03%)
max u_θ	1	0.99693 (∼0.31%)	0.9980 (∼0.20%)	0.99669 (∼0.33%)
max u_z	0.1454	0.14639 (∼0.68%)	0.1506 (∼3.57%)	0.14632 (∼0.63%)

With this test-case the well known linear first instability threshold of the Taylor–Couette flow is found. Also the nonlinear saturation is comparable to what is reported in the literature. The same topology of the flow is observed and quantitatively similar velocity magnitudes at the steady state are established. This makes us confident about the accuracy of the method in taking into account centrifugal, pressure and nonlinear effects in a bounded domain.

6.4. Magnetohydrodynamic Taylor–Couette flow

We now extend our validation to the test-case of the instability of an axisymmetric MHD Taylor–Couette flow with periodic boundary conditions in the axial direction. In this case the instability studied in the previous section is modified due to the presence of an axial magnetic field. An imposed constant axial field B_0 is added to the magnetic field. It is well known that such an axial magnetic field has a significant stabilizing effect. This phenomenon of delay in the appearance of the first Taylor–Couette instability was found by Chandrasekhar [32], confirmed by linear numerical calculations in [7] and by spectral numerical simulations [9,33]. The fluid flow will try to bend the axial magnetic field lines but the restoring Lorentz force will prevent the fluid motion, which stabilizes the flow profile.

To assess our numerical codes in this context, we evaluate the evolution of the axial kinetic energy as a function of the Hartmann number Ha, which measures the ratio between electrodynamic forces and viscous forces. The presence of a uniform magnetic field in the axial direction does not affect the profile of the stable azimuthal velocity that exists without the magnetic field, Eq. (26), which we choose as initial condition. The dimensionless geometric parameters, radius ratio ζ and aspect ratio Γ are the same as in the previous section. We introduce here the magnetic Prandtl number which is the ratio of viscosity and magnetic diffusivity. The dimensionless numbers describing the problem are then

$$Pr = \frac{\nu}{\lambda}, \qquad Re = \frac{U\mathcal{L}}{\nu}, \qquad Ha = \frac{B_0\mathcal{L}}{\sqrt{\mu_0\rho\nu\lambda}}, \qquad \zeta = \frac{R_{int}}{R_{ext}}, \qquad \Gamma = \frac{L_z}{\mathcal{L}}, \tag{40}$$

where μ_0 is the magnetic constant and ρ is the fluid density. The simulations are performed for $Pr = 1$, $Re = 100$, $\zeta = 0.5$ and $\Gamma = 4$. The resolution used is $N^3 = 128^3$, the penalization parameter $\eta = 5 \cdot 10^{-4}$ and the computational domain size is $L_x = L_y = 5\pi/2$ and $L_z = 2\pi$. For none of these calculations regularization of the velocity or magnetic field in the solid region (or mask) is used. The boundary conditions described in [7] are a fixed azimuthal velocity on the inner cylinder ($U = \Omega_{int} R_{int} = 1$), no-slip on the outer cylinder and perfectly conducting walls, so that the normal magnetic field at the wall and the axial and azimuthal current density vanish ($b_r = 0$ and $j_z = j_\theta = 0$) [7]. With these parameters the Taylor–Couette flow is hydrodynamically unstable, as was observed in the previous section. With the penalization method we can impose the vanishing radial magnetic field but the current density is not constrained.

The evolution of the axial kinetic energy varies as a function of the imposed magnetic field (or Hartmann number), for a fixed Reynolds number, as is shown in Fig. 20. These calculations allow us to determine the threshold for the instability. For $Re = 100$ the critical Hartmann number found is $Ha_c \approx 7.9$. Like in the previous section the threshold is determined by linear interpolation of the growth and decay rates. For $Re = 100$ the flow is hydrodynamically unstable and Taylor vortices should appear, but for $Ha > 7.9$, the instability is suppressed by the magnetic field.

In Fig. 21 we show the topology of the flow resulting of our simulation (cut in the r–z plane). This figure could be compared to Fig. 1 in [9]. This comparison is merely qualitative, since the ratio of the radii is $\zeta = 0.95$ in the cited reference and here we have used $\zeta = 0.5$. We have not tried to quantitatively study the same geometry, since our method is not particularly adapted for the case $\zeta = 0.95$, because a very large part of the computational domain would correspond to the mask. To obtain a reasonable number of grid-points in the fluid domain, extremely large resolutions would be needed. Immersed boundary methods with uniform space discretization are clearly not the most adapted tool for this aspect ratio. The parameters chosen in our simulation are $Pr = 1$, $Ha = 7$, $Re = 100$, $\zeta = 0.5$ and $\Gamma = 4$. Despite the different parameters for the two computations, the resulting hydromagnetic flow has a similar topology. We note how the magnetic lines are advected by the flow. The resulting restoring Lorentz force stabilizes the fluid.

With this test-case we therefore found the well known stabilizing effect of an axial magnetic field on the Taylor–Couette flow. Qualitatively the flow behavior is very similar to what is found in other investigations. We were not able to quantitatively compare with the literature since our boundary conditions on the magnetic field are not the same as in [9], where insulating boundaries are considered and also because, in this reference, the parameter ζ is larger. To compare with more accuracy our codes with the literature we treat in the following section a test case with boundary conditions and geometry which are adapted to our numerical method.

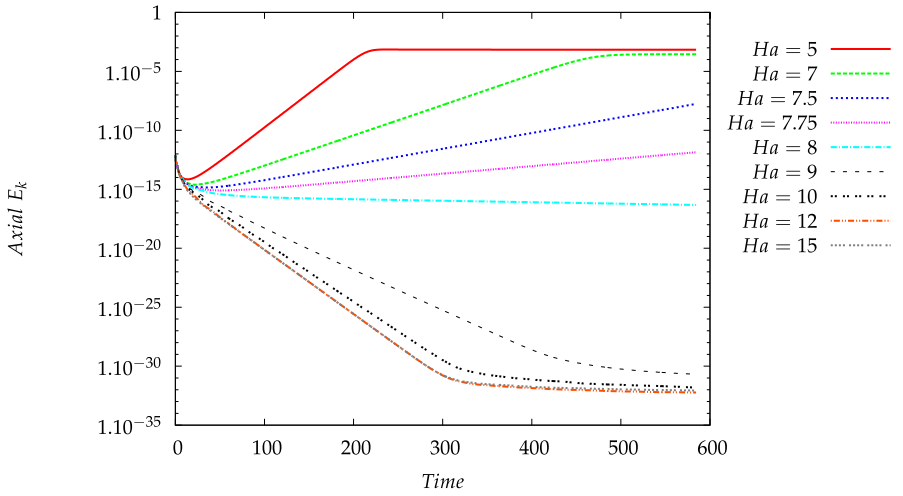

Fig. 20. Evolution of the axial kinetic energy for different Hartmann numbers.

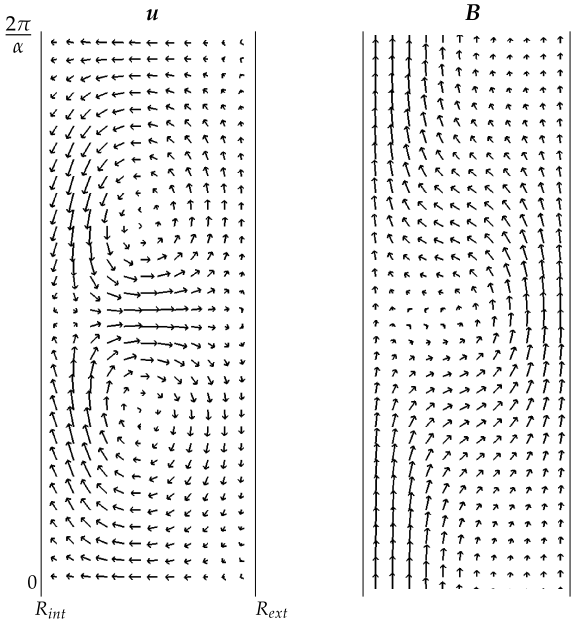

Fig. 21. Hydromagnetic flow. Cut in the r–z plane of velocity $\boldsymbol{u}$ (left) and magnetic ($\boldsymbol{B}$) field (right) for $Pr = 1$, $Ha = 7$, $Re = 100$, $\zeta = 0.5$ and $\Gamma = 4$.

6.5. Flow induced by a helical magnetic field

Shan, Montgomery and Chen [34] studied numerically a conductive fluid confined in a periodic cylinder where an axial electric and magnetic field are imposed, which results in a helical magnetic field (see Fig. 22). They used a spectral code which decomposed the fields into Chandrasekhar–Kendall orthonormal eigenfunctions of the curl. In that study they discovered a transition between an axisymmetric state with a zero velocity to a laminar helical state where a dynamic equilibrium appears, *i.e.*, a steady state with non-zero velocity.

The parameters chosen for the numerical study are selected to closely reproduce the simulations in [34]. A fixed axial magnetic field $B_0 = 4.5$ is imposed and the fluid has a constant magnetic diffusivity and kinematic viscosity $\lambda = \nu = 0.045$. The computational domain size is $L_x = L_y = 0.8\pi$ and $L_z = 8$. The typical length scale is the cylinder radius, $\mathcal{L} = R_0 = 1$, the axial length is $L_z = 8R_0$, the resolution used for the simulations is $N^3 = 128^3$ grid-points and the penalization parameter $\eta = 5 \cdot 10^{-4}$. Three dimensionless numbers characterize the system: the Lundquist number (S), the Hartmann number (Ha) and the pinch ratio for the axisymmetric zero flow state (Θ_0):

$$S = \frac{C_A \mathcal{L}}{\lambda}, \qquad Ha = \frac{B_0 \mathcal{L}}{\sqrt{\rho \mu_0 \lambda \nu}}, \qquad \Theta_0 = \frac{\overline{B_\theta}}{\langle B_z \rangle}, \tag{41}$$

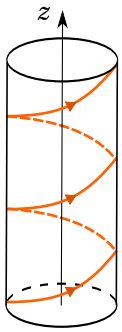

Fig. 22. Helical magnetic field scheme.

with C_A the axial Alfvén velocity $C_A = B_0/\sqrt{\rho\mu_0}$, $\overline{B_\theta}$ is the wall-averaged poloidal magnetic field and $\langle B_z \rangle$ is the volume-averaged axial magnetic field.

The transition between states is determined as a function of one of these dimensionless numbers, the pinch ratio Θ_0, which is varied by adjusting the imposed average axial electric field E_0 and which is directly linked to the poloidal magnetic field. The other dimensionless numbers are maintained constant, $S = Ha = 100$. For the parameters given above, the linear theory predicts a transition for an imposed electric field, $E_0 = 0.33$ [34,35].

To compare with Shan et al. we impose the same boundary conditions. The walls are treated as perfect conductors and are coated with a thin layer of insulator. Hereby both the radial magnetic and current density field vanish ($B_r = j_r = 0$). For the velocity field only the radial component vanishes at the wall. The penalization method is used to impose a vanishing normal component of the velocity ($\boldsymbol{u} \cdot \boldsymbol{n} = 0$) without any regularization technique. Also an azimuthal magnetic field B_{θ_0} is imposed via the penalization term. In this case the vanishing radial current density ($j_r = 0$) is automatically satisfied because the azimuthal magnetic field does not generate a radial current density (the r-component of the curl of the imposed magnetic field is zero). The boundary conditions are thus satisfied.

The way the electric field is imposed in our simulations differs from the simulations by Shan et al. In their simulations the electric field explicitly appears in the discretized equations, whereas in our case the electric field is indirectly imposed through the magnetic field at the wall (which can be related to the electric field using Stokes' theorem). This can lead to small differences in the transients, but is not expected to greatly affect the steady state solutions.

The azimuthal magnetic field $B_{\theta_0}(r)$ is imposed with the volume penalization method in the solid region using the regularization technique, like for the z-pinch case (see Section 5.2). The azimuthal magnetic field increases linearly with r from $r = R_0$ (the fluid–solid frontier) to $r = 0.34\pi$ and then smoothly tends to zero using an interpolating Hermite polynomial from $r = 0.34\pi$ to $r = 0.385\pi$. The periodicity of the computational region is hereby satisfied and the magnetic derivative of the base-field is continuous at the wall.

To validate the code we perform the same calculations done by Shan et al. We vary the axial current density (j_z) and we calculate E_0 when the simulation reaches a steady state using Ohm's law

$$E_0 = (-\boldsymbol{u} \times \boldsymbol{B})_z + \frac{j_z}{\sigma}. \tag{42}$$

We find (see Fig. 24) that the instability threshold between the axisymmetric and helical state is situated between $E_0 = 0.302$ and $E_0 = 0.355$ as found in [34]. The kinetic energy starts to grow when the imposed electric current is $E_0 = 0.355$. The growth rate of the energy is calculated using Alfvén time units ($t_A = t_{num} C_A / L_z$). A least-square fitting gives the growth rate of the kinetic energy as 0.54, corresponding to a growth rate of 0.27. This can be compared to the analytical value 0.279 calculated for an applied electric field $E_0 = 0.35$. Taking into account that our imposed magnetic field is slightly different (since the electric field is imposed indirectly in our case), the two different growth rates match in good order. In Fig. 23 the excited mode is visualized, which is a helical mode with azimuthal and axial mode numbers $m = n = 1$, respectively, as in [34].

Increasing the pinch ratio to $E_0 = 0.402$ the flow returns to its axisymmetric *copper-wire* solution, which is also observed for certain values in [34]. An explanation for this behavior is the shape of the instability curves in the Θ_0–Ha plane. By increasing the pinch ratio, different m, n helical modes appear at a fixed Ha, but they can disappear by increasing Θ_0 to even higher values. This was investigated in [36].

In the next figures, 25 to 28, we compare our different simulations with the ones performed by Shan et al. We find quantitatively the same evolution of the average current density and the total dissipation rate ($\varepsilon_T = \lambda \langle \boldsymbol{j}^2 \rangle + \nu \langle \boldsymbol{\omega}^2 \rangle$). These quantities are time averaged during the dynamical steady state, since the flow becomes chaotic, if the pinch ratio (or E_0) is large.

Some quantitative differences are observed in Figs. 25 and 26 for values around $E_0 = 0.6$. At that point both methods might not trigger exactly the same helical modes, since the electric field is imposed in a slightly different way. Both methods might therefore give results corresponding to different multi-mode states. When the pinch ratio is increased further, the deviations become smaller, as can be seen in Figs. 27 and 28.

Fig. 23. First helical mode, velocity streamlines colored with the axial velocity u_z. (For interpretation of colors in this figure, the reader is referred to the web version of this article.)

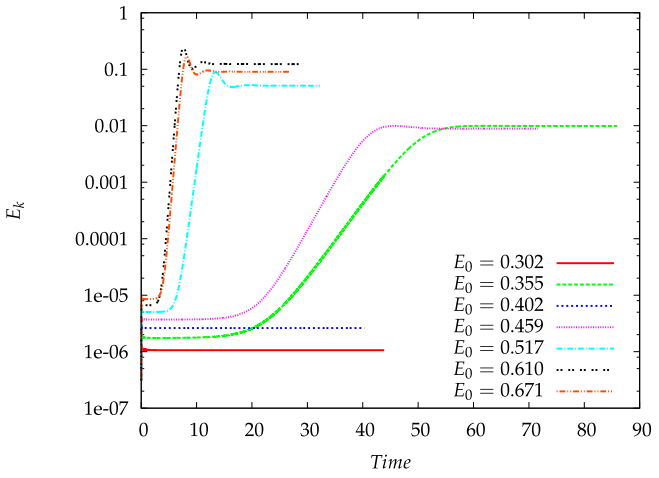

Fig. 24. Evolution of the kinetic energy for different imposed axial electric fields.

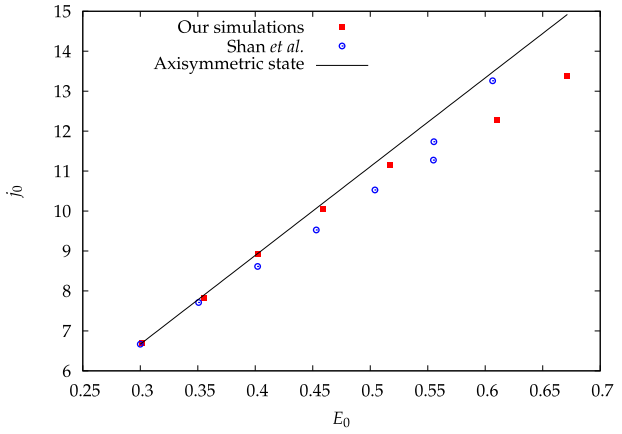

Fig. 25. Zoom: average axial current as a function of the average electric field.

This test-case allows us to validate the nonlinear MHD code with boundary conditions imposed on both the velocity and magnetic field. A linear analytical result is confirmed. The "multi-mode" and turbulent states that are observed in literature also appear in our simulations. Further simulations with varying Hartmann number to complete our picture of the nonlinear behavior of the system constitute an interesting perspective.

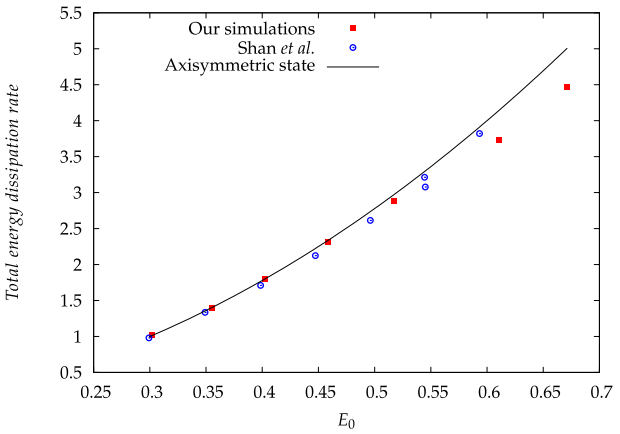

Fig. 26. Zoom: total energy dissipation rate as a function of the average electric field.

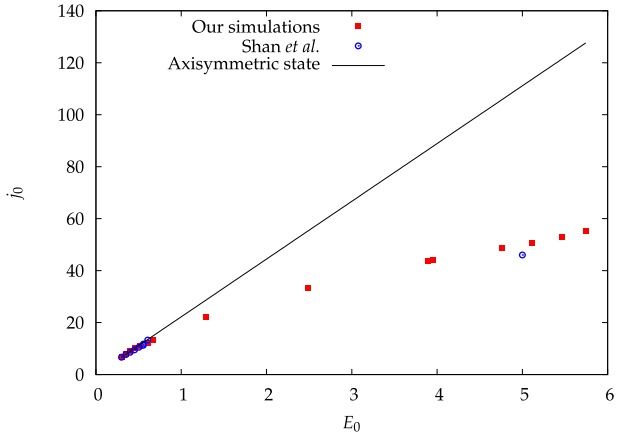

Fig. 27. Average axial current as a function of the average electric field.

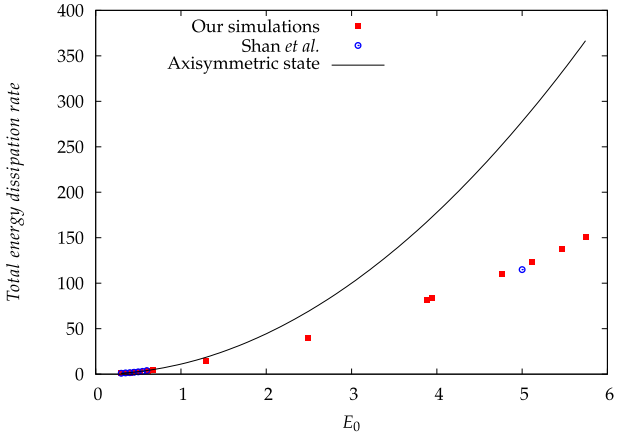

Fig. 28. Total energy dissipation rate as a function of the average electric field.

6.6. Magnetohydrodynamic simulation in an asymmetric toroidal geometry

To illustrate the potential of the volume penalization method to deal with complex geometries we perform an MHD simulation in a torus with a 'D' shape cross section (Fig. 29(a)). This shape is given by a parametric equation that is a modified version of the formula given by Manickam [37],

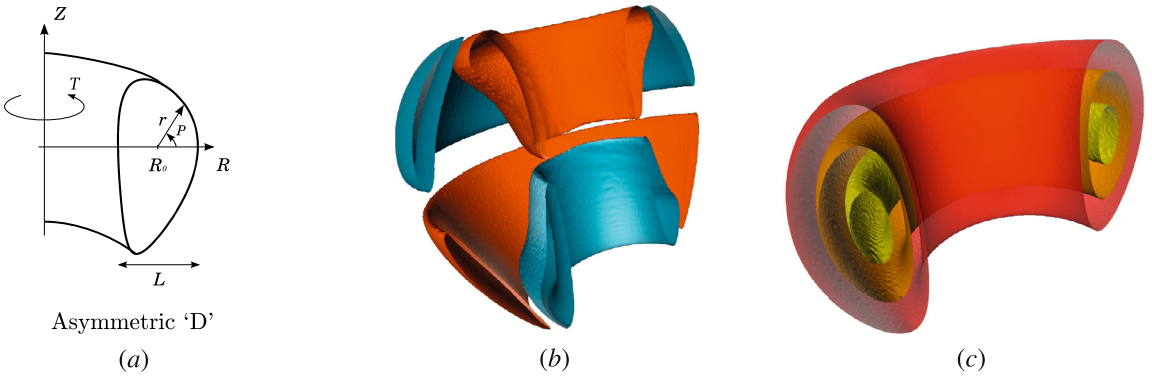

Fig. 29. (a) Asymmetric toroidal geometry, (b) toroidal velocity field component isocontours (blue $+9 \cdot 10^{-4}$, orange $-9 \cdot 10^{-4}$) and (c) perturbed toroidal magnetic field component isocontours (red $+0.025$, orange $+0.04$, yellow $+0.05$). (For interpretation of the references to color in this figure legend, the reader is referred to the web version of this article.)

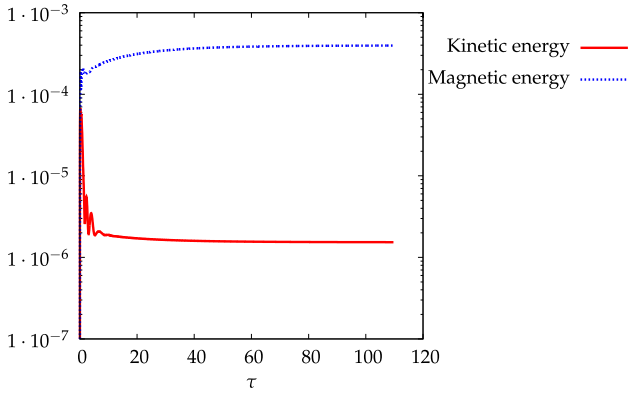

Fig. 30. Kinetic and perturbed magnetic energy time evolutions (in toroidal Alfvén unit times) for the magnetohydrodynamic toroidal simulation.

$$R(t) = \frac{L}{2}\big[\cos\big(t - \alpha + \delta \sin(t)\big)\cos(\zeta) - \kappa \sin(t)\sin(\zeta)\big], \tag{43}$$

$$Z(t) = \frac{L}{2}\big[\cos\big(t - \alpha + \delta \sin(t)\big)\sin(\zeta) + \kappa \sin(t)\cos(\zeta)\big], \tag{44}$$

with $t \in [0, 2\pi]$, δ the triangularity, κ the ellipticity, α the asymmetry and ζ the rotation angle. For the considered asymmetric cross section the following values of these parameters are chosen: $\delta = 0.5$, $\kappa = 2.1$, $\alpha = 0.4$ and $\zeta = 0.15$.

The initial condition for the simulations are zero magnetic perturbations and zero velocity. The simulation is carried out for a cubic domain of size $(2\pi)^3$ consisting of 256^3 grid points. We fix the penalization parameter to $\eta = 5 \cdot 10^{-4}$. The time step is adaptive and the chosen CFL coefficient is 0.1.

A helical magnetic field is imposed inside the torus. We take into account an imposed curl free toroidal magnetic field and an irrotational toroidal electric field. These two fields generate a Lorentz force that makes the magnetofluid move within the torus. In Fig. 29 ((b) and (c)) we present the velocity and the perturbed magnetic toroidal component isocontours at the steady state for a toroidal geometry with asymmetric cross section. The perturbed toroidal magnetic field is created by the velocities in the poloidal plane. This component of the magnetic field is important because it generates a toroidal Lorentz force that induces the toroidal velocities [38].

In Fig. 30 the evolution of the kinetic and perturbed magnetic energy is visualized. A steady state is obtained where the velocity field possesses a small fraction of the total energy. In real magnetic toroidal devices where the total energy is very important this small fraction is translated by a velocity of several kilometers per second. These velocities need to be taken into account to describe correctly the particle transport in such devices.

It was shown in [39] that a dominant toroidal velocity appears for decreasing dissipation. Also, breaking the up–down symmetry of the torus induces the development of a net toroidal flow.

The numerical method presented in this manuscript allows to easily modify the shape of a torus and to compare different geometries without remeshing. The magnetohydrodynamic results in a toroidal geometry change significantly depending on the boundary shape. This case, which is further discussed in [39], shows the flexibility of the present method for studies where the influence of the shape of the domain on the dynamics is investigated.

7. Conclusion

An extension and implementation of the penalization method into a pseudo-spectral Fourier code solving the MHD equations are presented. This penalization method, which allows the introduction of obstacles and walls in the computational domain, is implemented in different ways with respect to the numerical scheme and definition of the fields within the solid domains.

The numerical code is validated by comparison with several test-cases and theory. First in two dimensions the convergence of the results towards an analytical solution by decreasing the penalization parameter and increasing the resolution are shown. The method converges faster than second order if a regularization technique in the solid domain is applied which removes the discontinuities in the derivatives of the velocity and magnetic field at the solid–fluid boundary.

Then in three dimensions the first instability threshold of the hydrodynamic Taylor–Couette flow is found with good accuracy. Also the nonlinear saturation of this flow is compared and validated with the literature. For the MHD Taylor–Couette flow the current inability to impose non-homogeneous Neumann boundary conditions using the penalization method, makes the comparison of our numerical results with the literature difficult. A more appropriate test-case to validate the three-dimensional implementation of the penalization method to compute MHD flows is the flow induced by a helical magnetic field. This case is correctly reproduced. The linear threshold of the transition between an axisymmetric and a helical state is found. Also the evolution of the average axial current and the total dissipation rate as a function of the average electric field are compared with the literature and are in good agreement. Finally the computation of the MHD dynamics in a toroidal domain illustrates the flexibility of the numerical method.

All these test-cases allow us to validate the numerical method to solve correctly the MHD equations in a confined domain. The limitation are the restricted magnetic boundary conditions that can be applied. Presently, the current density can be only be imposed indirectly via the magnetic field. A modified volume penalization method that allows the introduction of non-homogeneous three-dimensional Neumann boundary conditions is currently being developed. We note that such a method is relevant to a wider domain of applications than MHD, *e.g.* in heat transfer to impose a given heat flux at the wall. One-dimensional results are presented in Appendix C.

Acknowledgements

We are very grateful to C. Jause-Labert, A. Delache, D. Kolomenskiy, F.S. Godeferd, S. Neffaa and M. Roberts for the parallelization of the numerical code and for the help with the pseudo-spectral and volume penalization methods. We acknowledge financial support from the French Research Agency (ANR), project SiCoMHD, contract ANR-11-BLAN-045, as well as IDRIS for computing time, project i2012021664 and i2013051664. We also extend our thanks to the 7th Festival de Théorie at Aix-en-Provence that allows us to have fruitful exchanges and discussions about the present work.

Appendix A. Asymptotic analysis of the penalized momentum and induction equations

This section follows the method used by Angot et al. [15] for the momentum equation in the hydrodynamic version. An asymptotic development of $\mathbf{u}$ and $\mathbf{B}$ with the small parameter η is done first and gives

$$\mathbf{u} = \mathbf{u}_0 + \eta\mathbf{u}_1 + \eta^2\mathbf{u}_2 + \eta^3\mathbf{u}_3 + \cdots, \tag{A.1}$$

$$\mathbf{B} = \mathbf{B}_0 + \eta\mathbf{B}_1 + \eta^2\mathbf{B}_2 + \eta^3\mathbf{B}_3 + \cdots. \tag{A.2}$$

Then these expressions are inserted into the governing equations (Eqs. (11) and (12))

$$\partial_t\mathbf{u} = -\mathbf{u}\cdot\nabla\mathbf{u} - \nabla\Pi + \nu\nabla^2\mathbf{u} + \mathbf{j}\times\mathbf{B} - \frac{\chi}{\eta}(\mathbf{u}-\mathbf{u}_{wall}), \tag{A.3}$$

$$\partial_t\mathbf{B} = \nabla\times(\mathbf{u}\times\mathbf{B}) + \lambda\nabla^2\mathbf{B} - \frac{\chi}{\eta}(\mathbf{B}-\mathbf{B}_{wall}) \tag{A.4}$$

and we identify the terms of the same order in η.

order -1

$$\begin{cases} 0 = -\dfrac{\chi}{\eta}(\mathbf{u}_0 - \mathbf{u}_{wall}) \\ 0 = -\dfrac{\chi}{\eta}(\mathbf{B}_0 - \mathbf{B}_{wall}) \end{cases} \Rightarrow \quad \text{if } \chi = 1 \begin{cases} \mathbf{u}_0 = \mathbf{u}_{wall} \\ \mathbf{B}_0 = \mathbf{B}_{wall} \end{cases} \tag{A.5}$$

At this order, in the solid domain the fields are equal to the boundary conditions.

order 0

$$\partial_t\mathbf{u}_0 = -\mathbf{u}_0\cdot\nabla\mathbf{u}_0 - \nabla\Pi_0 + \nu\nabla^2\mathbf{u}_0 + \nabla\times\mathbf{B}_0\times\mathbf{B}_0 - \frac{\chi}{\eta}\mathbf{u}_1, \tag{A.6}$$

$$\partial_t\mathbf{B}_0 = \nabla\times(\mathbf{u}_0\times\mathbf{B}_0) + \lambda\nabla^2\mathbf{B}_0 - \frac{\chi}{\eta}\mathbf{B}_1. \tag{A.7}$$

At this order, the Navier–Stokes and induction equations are found in the fluid ($\chi = 0$). In the solid domain ($\chi = 1$), the hypothesis that the fields of the order 0 are in a stationary state and homogeneous in space is made. In this case the equations reduce to

$$\nabla \Pi_0 = \frac{\chi}{\eta}\mathbf{u}_1, \qquad 0 = -\frac{\chi}{\eta}\mathbf{B}_1. \tag{A.8}$$

The first equation is Darcy's law. It is easily deduced that the penalization parameter η must tend to zero for the velocity field to converge to the boundary condition value. The equation for the magnetic field remains not interpreted at the time.

order 1

$$\partial_t \mathbf{u}_1 = -\mathbf{u}_0 \cdot \nabla \mathbf{u}_1 - \nabla \Pi_1 + \nu \nabla^2 \mathbf{u}_1 + \nabla \times \mathbf{B}_1 \times \mathbf{B}_0 - \frac{\chi}{\eta}\mathbf{u}_2, \tag{A.9}$$

$$\partial_t \mathbf{B}_1 = \nabla \times (\mathbf{u}_1 \times \mathbf{B}_0) + \nabla \times (\mathbf{u}_0 \times \mathbf{B}_1) + \lambda \nabla^2 \mathbf{B}_1 - \frac{\chi}{\eta}\mathbf{B}_2. \tag{A.10}$$

Here the same hypothesis about the order 0 fields is made. There is no interpretation for this system, but we see that the system cannot be closed and we should truncate the series to do so.

Appendix B. Analysis of the Hermite regularization

In this section an analysis of the one-dimensional penalized Poisson equation imposing Dirichlet boundary condition is conducted, and the order of convergence yielded by the Hermite regularization method will be characterized and compared to the classical penalization.

The unpenalized problem in $[-1; 0]$ reads:

$$\begin{cases} -u'' = 0 \\ u(-1) = 0, \quad u(0) = \dfrac{1}{2} \end{cases}$$

The penalized problem is solved in the interval $[-1; 1]$:

$$\begin{cases} -u'' = -\dfrac{\chi}{\eta}(u - u_{wall}) \\ u(-1) = 0, \quad u(1) = u_{wall}(1) \end{cases} \quad \text{with} \quad \chi = \begin{cases} 0 & \text{in } \Omega_f = [-1; 0[\\ 1 & \text{in } \Omega_s = [0; 1] \end{cases} \tag{B.1}$$

At the fluid–solid interface we impose the continuity condition $u_s(x) = u_f(x)$, $u_s'(x) = u_f'(x)$ for $x = 0$.

For the classical penalization, we set $u_{wall} = \frac{1}{2}$ and thus $u_{wall}(1) = \frac{1}{2}$. The solutions are

$$\begin{cases} u_f(x) = a(x+1), \quad u_s(x) = K_1 e^{\frac{x}{\sqrt{\eta}}} + K_2 e^{\frac{-x}{\sqrt{\eta}}} + \dfrac{1}{2} \\ \text{with} \quad a = \dfrac{\alpha(e_*^2 - 1)}{2(\alpha - 1 - e_*^2 - e_*^2\alpha)} + \dfrac{1}{2} \\ \text{and} \quad K_1 = \dfrac{-\alpha}{2(\alpha - 1 - e_*^2 - e_*^2\alpha)}, \quad K_2 = \dfrac{\alpha e_*^2}{2(\alpha - 1 - e_*^2 - e_*^2\alpha)} \end{cases}$$

where $\alpha = \sqrt{\eta}$ and $e_* = e^{\frac{1}{\sqrt{\eta}}}$. The subscripts 's' and 'f' stand for the solid and the fluid domain, respectively.

For the penalization with the regularization method, the interpolating polynomial must be defined first. An Hermite interpolation consists in finding a polynomial which fits two separate points where the values of the function and of a chosen number of derivatives are imposed. In our case the Hermite polynomial $H(x)$ must match the values of u and its first derivative at $x = 0$ and yields $H(1) = H'(1) = 0$ at $x = 1$. As the exact solution of the unpenalized problem is $u(x) = \frac{x+1}{2}$, the expression of the third degree Hermite polynomial can be easily derived:

$$\begin{cases} H(0) = \dfrac{1}{2}, \quad H'(0) = \dfrac{1}{2}, \quad H(1) = 0, \quad H'(1) = 0 \\ H(x) = \dfrac{3x^3}{2} - \dfrac{5x^2}{2} + \dfrac{x}{2} + \dfrac{1}{2} \end{cases}$$

In Eq. (B.1), $H(x)$ is set as u_{wall} and, with the same notations as before, the solutions are

$$\begin{cases} u_f(x) = a(x+1), \quad u_s(x) = K_1 e^{\frac{x}{\sqrt{\eta}}} + K_2 e^{\frac{-x}{\sqrt{\eta}}} + H(x) + (9x - 5)\eta \\ \text{with} \quad a = \dfrac{14\alpha^3(1 - e_*^2) + 8\alpha^2 e}{\alpha - 1 - e_*^2 - e_*^2\alpha} + \dfrac{1}{2} - 5\alpha^2 \\ \text{and} \quad K_1 = \dfrac{14\alpha^3 + 4\alpha^2 e_*(\alpha + 1)}{\alpha - 1 - e_*^2 - e_*^2\alpha}, \quad K_2 = \dfrac{-14\alpha^3 e_*^2 - 4\alpha^2 e_*(\alpha - 1)}{\alpha - 1 - e_*^2 - e_*^2\alpha} \end{cases}$$

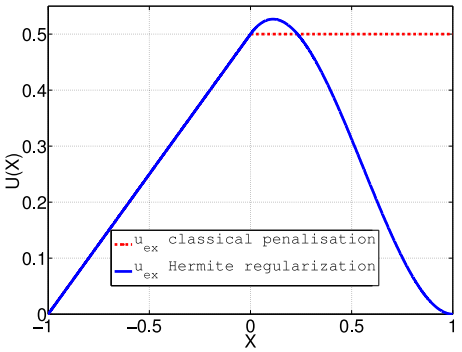

Fig. B.31. Exact solution with the different penalization methods. With the regularization method, the solution is C^1 on the whole domain.

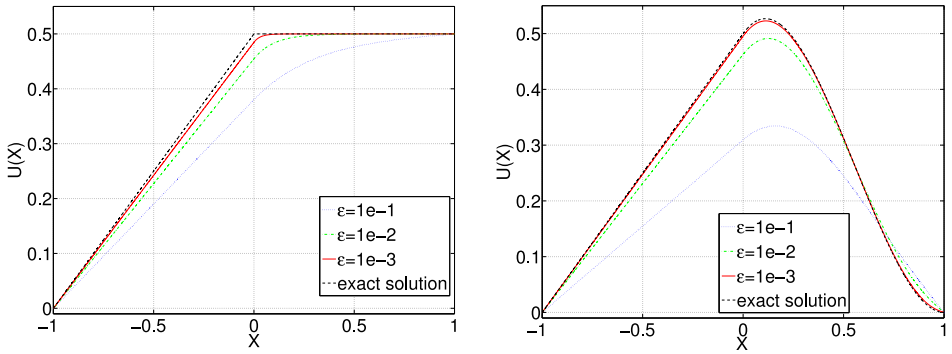

Fig. B.32. Solutions of the penalized problem for various values of η for the classical (left) and regularized penalization method (right).

Fig. B.31 shows the exact profiles of the solution of the Poisson equation in $[-1, 0[$ and the penalization term in $[0, 1]$. The solution of the penalized problem should converge to these profiles when $\eta \to 0$.

These solutions are compared to the exact solutions $u_f = \frac{x+1}{2}$ and $u_s = \frac{1}{2}$ in Fig. B.32 for different values of the penalization parameter η. It can be seen that both converge rapidly to the theoretical solutions when η becomes smaller.

From Fig. B.33, the same can be observed for the first derivative (top). The second derivatives (bottom) do not fit very well but the results are smoother in the case of the Hermite interpolation. Eventually the class of the function is increased with the second method, as expected.

B.1. Evaluation of the error

The penalization error in the L_2 norm can be computed directly as

$$\|\epsilon\|_2^2 = \int_{-1}^{0} (u_\eta - u_{exact})^2 dx = \int_{-1}^{0} \left(a(x+1) - \frac{x+1}{2} \right)^2 dx = \frac{(1-2a)^2}{12}$$

Then the coefficient a is replaced by the corresponding expressions obtained above in the two cases and the error becomes:

$$\begin{cases} \|\epsilon\|_2 = \left| \dfrac{(1-2a)}{\sqrt{12}} \right| \\ \text{classical penalization} : \|\epsilon\|_2 = \dfrac{\sqrt{\eta}}{\sqrt{12}} \\ \text{Hermite penalization} : \|\epsilon\|_2 = \dfrac{10\eta}{\sqrt{12}} \end{cases}$$

The convergence results are confirmed by the numerical experiments shown in Fig. B.34. The penalized solutions are plotted for several values of $\eta = [10^{-1}, 10^{-2}, 10^{-3}, 10^{-4}, 10^{-5}]$ and the errors with respect to the exact profiles are computed in the L_2 and L_∞ norms. The order of convergence is indeed improved to η for the regularization method instead of $\sqrt{\eta}$ with the classical penalization.

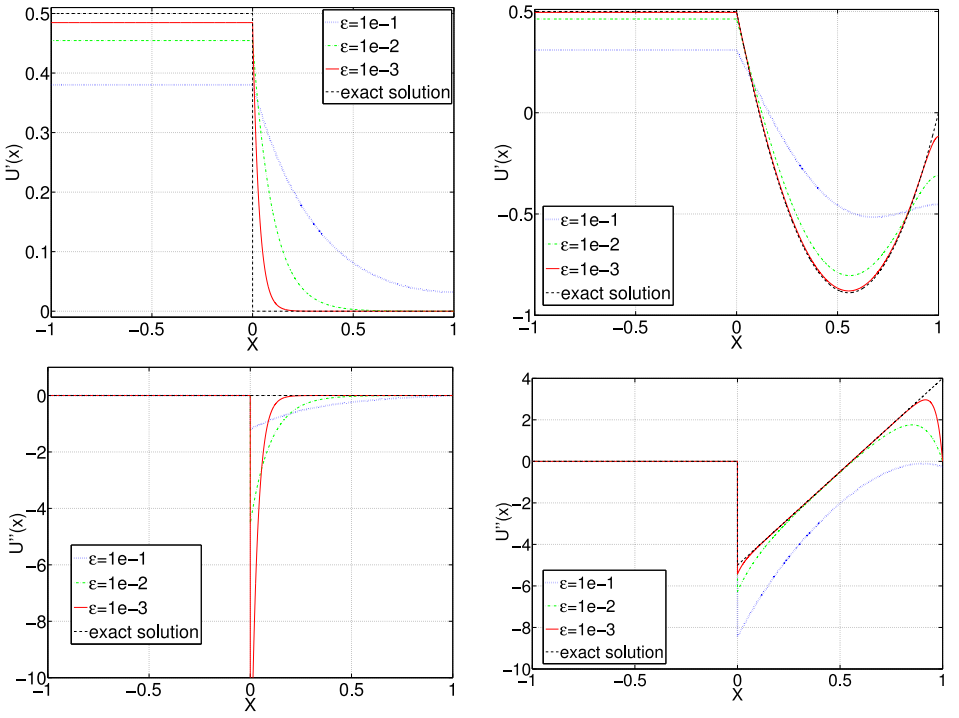

Fig. B.33. First (top) and second derivative (bottom) of the solution of the penalized problem for the classical (left) and regularized penalization method (right).

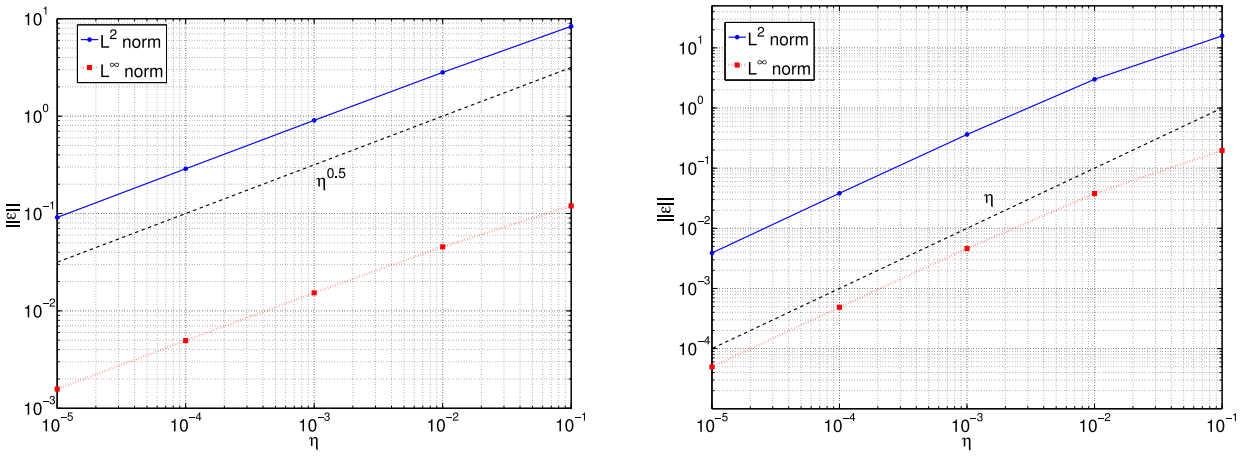

Fig. B.34. Penalization errors of u_η as a function of η for classical (left) and regularized penalization method (right).

The errors are also presented for the first and second derivative (Fig. B.35). It must be noticed that the error for the second derivative in the case of the regularized penalization method still improves when η decreases, whereas it increases for the classical method.

The order of convergence obtained in Sections 5.1 and 5.2 is higher than the one obtained here. This could result from the dissipative terms in the Navier–Stokes and induction equations, which are not present here. This term smoothens the remaining discontinuities and improves the order of convergence. The principal drawback of this method is that a baseflow must be known to precompute the regularization term. Moreover, it is possible that this baseflow is not continuous if in the numerical solution instabilities appear. As further perspective, this method should be implemented actively so that the regularization term fits the numerical solution as closely as possible at each time-step.

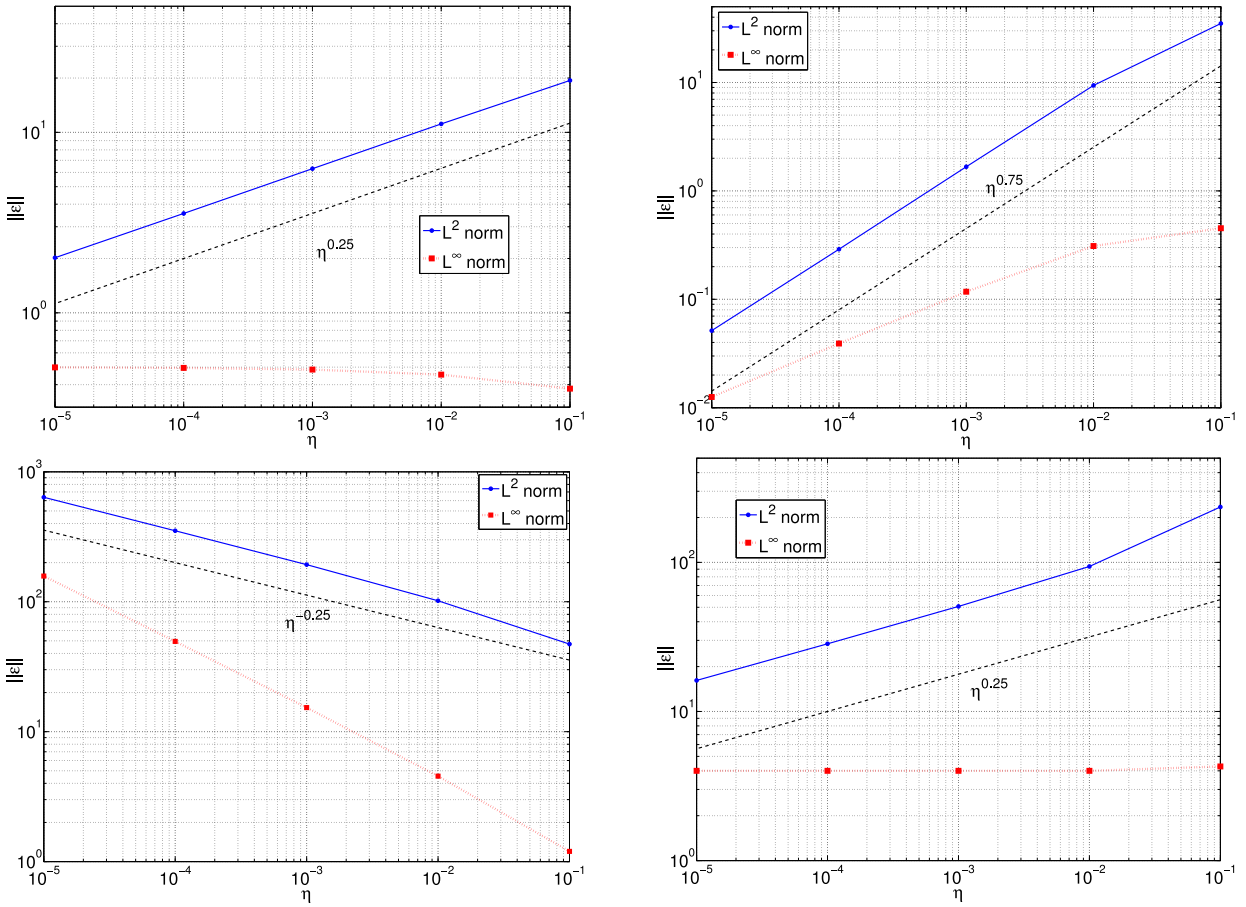

Fig. B.35. Penalization errors of u'_η (top) and u''_η (bottom) as a function of η for classical (left) and regularized penalization method (right).

Appendix C. Imposing non-homogeneous Neumann conditions with a penalization method

A generalization of the volume penalization method to impose non-homogeneous Neumann boundary conditions will be explained in the following.

The advection–diffusion equation of a scalar field $\theta(t, \boldsymbol{x})$ is considered in a domain Ω,

$$\frac{\partial \theta}{\partial t} + u_j \partial_j \theta = \alpha \Delta \theta, \tag{C.1}$$

$$\nabla \theta|_{\partial\Omega} = \gamma_{wall}, \quad \theta(t=0, \boldsymbol{x}) = f_0(\boldsymbol{x}). \tag{C.2}$$

Taking the gradient of this equation we can obtain a system of advection–diffusion equations for the different components of the gradient of θ, denoted by $\gamma_i = \partial_i \theta$. The penalization term is added and inhomogeneous Dirichlet conditions are imposed on γ_i,

$$\frac{\partial \gamma_i}{\partial t} + \partial_i (u_j \partial_j \theta) = \alpha \Delta \gamma_i - \frac{\chi(\boldsymbol{x})}{\eta} (\gamma_i - \gamma_{i_{wall}}). \tag{C.3}$$

We use a Fourier pseudo-spectral method and thus periodic boundary conditions are applied in the computational domain.

The next step is to integrate this last equation in space to recover the equation for θ. To do so we apply the divergence operator to the system of Eqs. (C.3). Using the relation $\nabla \cdot (\nabla f) = \Delta f$, the Laplace operator appears in the equation. Thus to recover the equation for θ a Poisson equation has to be solved. In spectral space this is equivalent to multiply Eq. (C.3) by the operator $-\imath k_i / k^2$,

$$\hat{\theta}(\boldsymbol{k}) = \frac{-\imath k_i}{k^2} \hat{\gamma}_i(\boldsymbol{k}), \tag{C.4}$$

with $k \neq 0$. In consequence, in physical space, the advection–diffusion equation with the penalization term for the gradient, can be written:

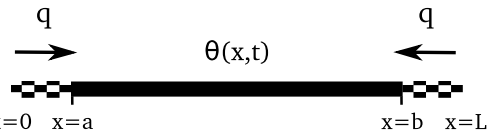

Fig. C.36. Scheme of the one dimensional diffusion problem for positive heat fluxes at the boundaries.

$$\frac{\partial\theta}{\partial t} + u_j\partial_j\theta = \alpha\Delta\theta + \mathcal{F}^{-1}\left[\frac{\imath k_i}{k^2}\mathcal{F}\left\{\frac{\chi(\boldsymbol{x})}{\eta}(\gamma_i - \gamma_{i_{wall}})\right\}\right]. \tag{C.5}$$

This last equation can be solved numerically with a pseudo-spectral method and the solution of the advection–diffusion equation with non-homogeneous Neumann boundary conditions can thus be obtained.

To verify this numerical method a one-dimensional test case is presented in the next section considering an instationary diffusion problem with non-homogeneous Neumann boundary conditions. A different numerical method to take into account homogeneous boundary conditions using spectral methods is presented in [23].

C.1. Test case: one-dimensional instationary diffusion problem

We consider the instationary diffusion equation for the temperature $\theta(x,t)$, with a positive heat flux on the left and right boundaries (see Fig. C.36). The equation to be solved is the following,

$$\frac{\partial\theta(x,t)}{\partial t} = \nabla^2\theta(x,t), \tag{C.6}$$

completed with non-homogeneous Neumann boundary conditions at $x=a$ and $x=b$,

$$\left.\frac{\partial\theta}{\partial x}\right|_{x=a} = -q \quad \text{and} \quad \left.\frac{\partial\theta}{\partial x}\right|_{x=b} = q. \tag{C.7}$$

The solution of this system is a combination of a parabolic function in space and a linear time evolution,

$$\theta(x,t) = q(x-a)\left(\frac{(x-a)}{(b-a)} - 1\right) + \frac{2q}{(b-a)}t. \tag{C.8}$$

The initial condition chosen for the simulation is the parabolic function that respects the inhomogeneous boundary conditions,

$$\theta(x,0) = q(x-a)\left(\frac{(x-a)}{(b-a)} - 1\right). \tag{C.9}$$

Numerically the diffusion equation is advanced in time and the two non-homogeneous Neumann boundary conditions are taken into account with a penalization term,

$$\frac{\partial\theta(x,t)}{\partial t} = \Delta\theta(x,t) + \underbrace{\mathcal{F}^{-1}\left[\frac{\imath k_i}{k^2}\mathcal{F}\left\{\frac{\chi(x)}{\eta}\left(\gamma_i(x) - \gamma_{i_{wall}}(x)\right)\right\}\right]}_{\text{Non-homogeneous Neumann BC term}}. \tag{C.10}$$

In Fig. C.36 the external region (small rectangles) and the internal region (black line) are visualized. On the border of the domain the periodicity must be ensured and therefore a zero gradient of θ is imposed at $x=0$ and $x=L$. For this reason we impose a linear evolution of the gradient $(\gamma_{i_{wall}}(x))$ in the solid region,

$$\gamma_{i_{wall}}(x)\big|_{x\in[0,a]} = \frac{-q}{a}x, \qquad \gamma_{i_{wall}}(x)\big|_{x\in[b,L]} = \frac{q}{L-b}(L-x). \tag{C.11}$$

Hence we verify the Neumann boundary conditions at $x=a$ and $x=b$, as well as the periodicity at the boundary of the computational domain.

We obtain numerically the solution of the diffusion equation (C.6) with the imposed Neumann boundary conditions. The computations are performed in a domain size $L=2\pi$ taking into account different resolutions N and penalization parameters η. The numerical error for the gradient of the temperature $\nabla\theta$ is calculated. The time evolution of the L_2-norm error is presented, for different values of N and η, in Fig. C.37. The error remains constant for $t>4$. A series of computations has been carried out either for fixed values of $\eta = 4\cdot 10^{-4}$ and varying N or for fixed $N=128$ and varying η.

At the steady state (when the error between the numerical results and the exact solution is constant in time) we can evaluate the different error norm and compute their convergence as a function of the penalization parameter and the resolution. Fig. C.38 presents the convergence of two error norms with η. Second order convergence of the L_2 error and a first order of the L_∞ norm are obtained when the penalization tends to zero. With the resolution (Fig. C.39) we observe a fourth order convergence for L_2 and a second order for the L_∞ error.

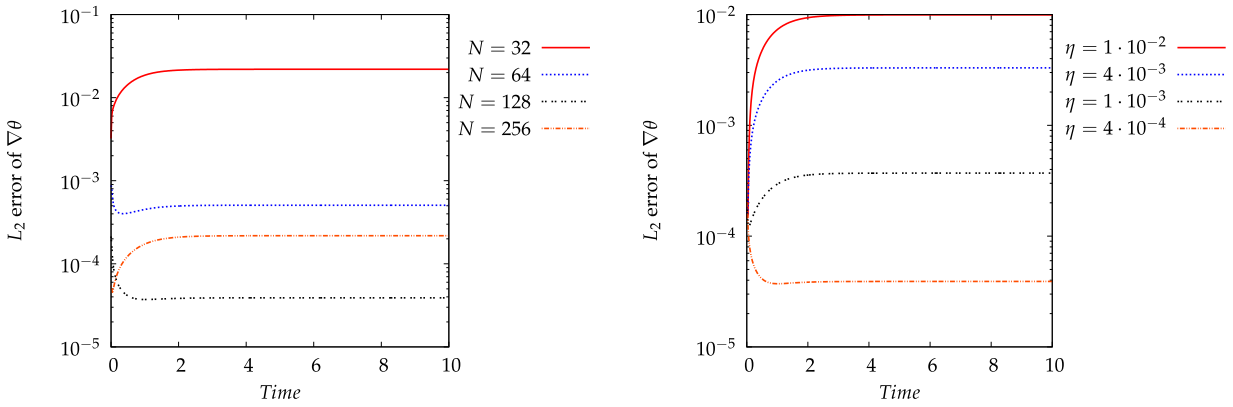

Fig. C.37. Time evolution of the L_2 error for the gradient of θ, between the numerical results and the exact solution, for different resolutions, N (left) and penalization parameters, η (right).

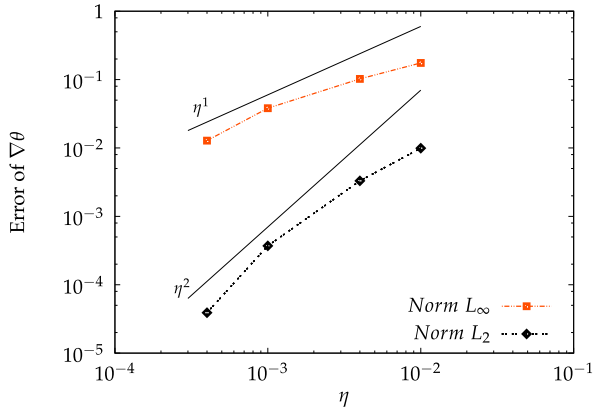

Fig. C.38. Evolution of the L_∞ and L_2 errors for the gradient of θ as a function of the penalization parameters (η).

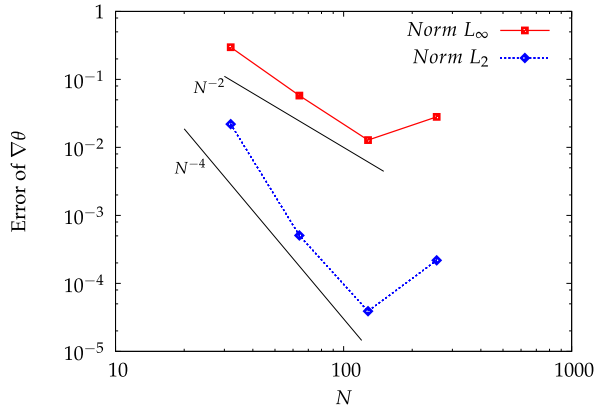

Fig. C.39. Evolution of the L_∞ and L_2 errors for the gradient of θ as a function of the grid points (N).

Appendix D. Corresponding explicit scheme of the semi-implicit penalization method

Jause-Labert et al. [24] extended an implicit formulation for the time-integration scheme for Dirichlet conditions, originally proposed by Kolomenskiy and Schneider [17] for Burgers' equation, to relax the constraint on the choice of the time-step. Their approach is discussed in some detail in this section. We use the following form of the penalized Navier–Stokes equation:

$$\partial_t u = \xi - \partial_x P - \frac{\chi}{\eta} u, \tag{D.1}$$

in this equation $u_{wall} = 0$, $P + u^2/2 \to P$ and ξ represents the nonlinear term. The viscous term can simply be added in the integral form, $u \exp(-\nu k^2 t) \to u$. In Fourier space we can write

$$\partial_t \hat{u} = P_\perp \left(\hat{\xi} - \frac{1}{\eta} \widehat{\chi u} \right), \tag{D.2}$$

with $P_\perp$ the Riesz projection-operator. The implicit treatment for the penalization term at the first order implies

$$\frac{\hat{u}^{n+1} - \hat{u}^n}{\Delta t} = P_\perp \left(\hat{\xi}^n - \frac{1}{\eta} \widehat{\chi u}^{n+1} \right), \tag{D.3}$$

the fact that in the last term the $\hat{\chi}$ is convoluted with $\hat{u}^{n+1}$ makes it non-trivial to write the implicit formulation. The following formulation is proposed [24]:

$$\hat{u}^{n+1} = P_\perp \mathcal{F} \left(\frac{u^n + \Delta t \, \mathcal{F}^{-1}[P_\perp \hat{\xi}^n]}{1 + \frac{\chi^{n+1}}{\eta} \Delta t} \right). \tag{D.4}$$

We know that the χ function takes only the values 0 and 1 depending if we are in the fluid or in the solid region respectively,

$$\chi(\boldsymbol{x}, t) = \begin{cases} 0 & \text{for } \boldsymbol{x} \in \Omega_f, \text{ the fluid domain} \\ 1 & \text{for } \boldsymbol{x} \in \Omega_s, \text{ the solid domain.} \end{cases} \tag{D.5}$$

An equivalent form of Eq. (D.4) can be written as follows

$$\hat{u}^{n+1} = P_\perp \mathcal{F} \left[\left(u^n + \Delta t \, \mathcal{F}^{-1}\left[P_\perp \hat{\xi}^n \right] \right) \left(1 - \chi^{n+1} \frac{\Delta t}{\eta + \Delta t} \right) \right]. \tag{D.6}$$

We recover the Navier–Stokes equation in the fluid domain and the implicit penalized equation (D.4) in the solid region. Using the following relations

$$\begin{aligned} &P_\perp P_\perp \hat{a} = P_\perp \hat{a} \\ &P_\perp \hat{u} = \hat{u}, \end{aligned} \tag{D.7}$$

the differential form of Eq. (D.6) can be written

$$\partial_t \hat{u} = P_\perp \left(P_\perp \hat{\xi} - \frac{\widehat{\chi u}}{\eta + \Delta t} - \frac{\Delta t}{\eta + \Delta t} \mathcal{F}\left\{ \chi \, \mathcal{F}^{-1}[P_\perp \hat{\xi}] \right\} \right). \tag{D.8}$$

Here we can identify two extreme cases. If $\Delta t \ll \eta$ Eq. (D.8) converges towards Eq. (D.2), we recover the classical penalized Navier–Stokes equation. On the other hand if $\eta \ll \Delta t$ we recover the following equation:

$$\partial_t \hat{u} = P_\perp \left(\mathcal{F}\left\{ (1 - \chi) \mathcal{F}^{-1}[P_\perp \hat{\xi}] \right\} - \frac{\widehat{\chi u}}{\Delta t} \right). \tag{D.9}$$

This equation is very close to the classical penalized Navier–Stokes equation. Here the time step Δt replaces the penalization parameter (η) and the nonlinear term vanishes in the solid region.

The semi-implicit penalization method is in this limit analogous to an explicit formulation. The difference is that, if the penalization parameter is small enough, the porosity of the solid walls is given by the value of the time step.

References

[1] P.A. Davidson, An Introduction to Magnetohydrodynamics, Cambridge Univ. Press, 2001.
[2] C. Suplee, The Plasma Universe, Cambridge Univ. Press, 2009.
[3] S.C. Jardin, Review of implicit methods for the magnetohydrodynamic description of magnetically confined plasmas, J. Comput. Phys. 231 (3) (2012) 822–838.
[4] J.-L. Guermond, R. Laguerre, J. Léorat, C. Nore, An interior penalty Galerkin method for the MHD equations in heterogeneous domains, J. Comput. Phys. 221 (1) (2007) 349–369.
[5] A.B. Iskakov, S. Descombes, E. Dormy, An integro-differential formulation for magnetic induction in bounded domains: boundary element-finite volume method, J. Comput. Phys. 197 (2) (July 2004) 540–554.
[6] K. Reuter, F. Jenko, C.B. Forest, R.A. Bayliss, A parallel implementation of an MHD code for the simulation of mechanically driven, turbulent dynamos in spherical geometry, Comput. Phys. Commun. 179 (4) (2008) 245–249.
[7] G. Rüdiger, D. Shalybkov, Stability of axisymmetric Taylor–Couette flow in hydromagnetics, Phys. Rev. E 66 (1) (2002) 016307.
[8] C. Gissinger, H. Ji, J. Goodman, Instabilities in magnetized spherical Couette flow, Phys. Rev. E 84 (2) (2011) 026308.
[9] A.P. Willis, C.F. Barenghi, Hydromagnetic Taylor–Couette flow: numerical formulation and comparison with experiment, J. Fluid Mech. 463 (1) (2002) 361–375.
[10] X. Shan, D.C. Montgomery, H. Chen, Nonlinear magnetohydrodynamics by Galerkin-method computation, Phys. Rev. A 44 (10) (November 1991) 6800.
[11] P.D. Mininni, D.C. Montgomery, Magnetohydrodynamic activity inside a sphere, Phys. Fluids 18 (2006) 116602.
[12] C.S. Peskin, The immersed boundary method, Acta Numer. 11 (1) (2002) 479–517.

[13] E. Arquis, J.-P. Caltagirone, Sur les conditions hydrodynamiques au voisinage d'une interface milieu fluide–milieux poreux : application à la convection naturelle, C. R. Acad. Sci. 299 (1984) 1–4.
[14] P. Angot, J.-P. Caltagirone, New graphical and computational architecture concept for numerical simulation on supercomputers, in: Proc. of 2nd World Cong. on Comp. Mech., vol. 1 (8), 1990, pp. 973–976.
[15] P. Angot, C.H. Bruneau, P. Fabrie, A penalization method to take into account obstacles in viscous flows, Numer. Math. 81 (1999) 497–520.
[16] K. Schneider, Numerical simulation of the transient flow behaviour in chemical reactors using a penalisation method, Comput. Fluids 34 (10) (December 2005) 1223–1238.
[17] D. Kolomenskiy, K. Schneider, A Fourier spectral method for the Navier–Stokes equations with volume penalization for moving solid obstacles, J. Comput. Phys. 228 (May 2009) 5687–5709.
[18] W.J.T. Bos, S. Neffaa, K. Schneider, Rapid generation of angular momentum in bounded magnetized plasma, Phys. Rev. Lett. 101 (23) (2008) 235003.
[19] S. Neffaa, W.J.T. Bos, K. Schneider, The decay of magnetohydrodynamic turbulence in a confined domain, Phys. Plasmas 15 (2008) 092304.
[20] W.J.T. Bos, S. Neffaa, K. Schneider, Self-organization and symmetry-breaking in two-dimensional plasma turbulence, Phys. Plasmas 17 (2010) 092302.
[21] C. Canuto, M.Y. Hussaini, A. Quarteroni, T.A. Zang, Spectral Methods in Fluid Dynamics, Springer, 1987.
[22] G. Carbou, P. Fabrie, Boundary layer for a penalization method for viscous incompressible flow, Adv. Differ. Equ. 8 (2003) 1453.
[23] B. Kadoch, D. Kolomenskiy, P. Angot, K. Schneider, A volume penalization method for incompressible flows and scalar advection–diffusion with moving obstacles, J. Comput. Phys. 231 (12) (2012) 4365–4383.
[24] C. Jause-Labert, F.S. Godeferd, B. Favier, Numerical validation of the volume penalization method in three-dimensional pseudo-spectral simulations, Comput. Fluids 67 (2012) 41–56.
[25] G.I. Taylor, Stability of a viscous liquid contained between two rotating cylinders, Philos. Trans. R. Soc. Lond. 223 (1923) 289–343.
[26] S. Laizet, E. Lamballais, High-order compact schemes for incompressible flows: a simple and efficient method with quasi-spectral accuracy, J. Comput. Phys. 228 (16) (2009) 5989–6015.
[27] C. Guthmann, J.M. Rax, Physique des Plasmas, Dunod, 2005.
[28] P.D. Mininni, A.G. Pouquet, D.C. Montgomery, Small-scale structures in three-dimensional magnetohydrodynamic turbulence, Phys. Rev. Lett. 97 (24) (December 2006) 1–4.
[29] J.-L. Guermond, J. Léorat, C. Nore, A new finite element method for magneto-dynamical problems: two-dimensional results, Eur. J. Mech. B, Fluids 22 (6) (December 2003) 555–579.
[30] R. Laguerre, C. Nore, J. Léorat, J.-L. Guermond, Induction effects in isolated axisymmetric conductors using a new finite element method, in: Proc. of the Summer Program, 2004, p. 1.
[31] J.-L. Guermond, R. Laguerre, J. Léorat, C. Nore, Nonlinear magnetohydrodynamics in axisymmetric heterogeneous domains using a Fourier/finite element technique and an interior penalty method, J. Comput. Phys. 228 (8) (2009) 2739–2757.
[32] S. Chandrasekhar, Hydrodynamic and Hydromagnetic Stability, Dover Publications, 1961.
[33] A.P. Willis, C.F. Barenghi, Hydromagnetic Taylor–Couette flow: wavy modes, J. Fluid Mech. 472 (2002) 399–410.
[34] X. Shan, D.C. Montgomery, H. Chen, Nonlinear magnetohydrodynamics by Galerkin-method computation, Phys. Rev. A 44 (10) (1991) 6800–6818.
[35] D.C. Montgomery, L. Phillips, M.L. Theobald, Helical, dissipative, magnetohydrodynamic states with flow, Phys. Rev. A 40 (3) (1989) 1515.
[36] X. Shan, D.C. Montgomery, Global searches of Hartmann-number-dependent stability boundaries, Plasma Phys. Control. Fusion 35 (1993) 1019.
[37] J. Manickam, Stability of $n = 1$ internal modes in tokamaks, Nucl. Fusion 24 (5) (1984) 595.
[38] L.P. Kamp, D.C. Montgomery, Toroidal flows in resistive magnetohydrodynamic steady states, Phys. Plasmas 10 (2003) 157.
[39] J.A. Morales, W.J.T. Bos, K. Schneider, D.C. Montgomery, Intrinsic rotation of toroidally confined magnetohydrodynamics, Phys. Rev. Lett. 109 (2012) 175002.